JCTC Journal of Chemical Theory and Computation

Open Access
This article is licensed under CC-BY-NC-ND 4.0

pubs.acs.org/JCTC Article

Unraveling the Ultrafast Photodynamics of Molecular Photoswitches in β-Adrenergic Receptors by First-Principles Nonadiabatic Dynamics Simulations

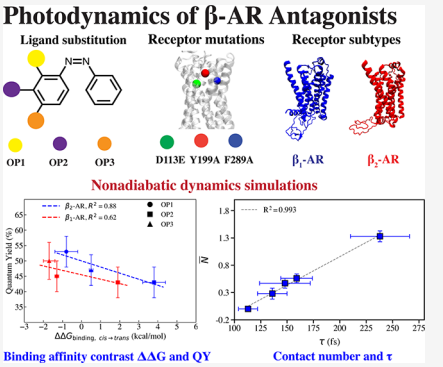
Published as part of Journal of Chemical Theory and Computation special issue "Modeling the Impact of Protein Mutations on Chemical Reactions for Biochemistry, Protein Engineering, and Drug Discovery".

Mohammad Khavani,[†] Amirhossein Bakhtiiari,[†] and Ruibin Liang*

Cite This: https://doi.org/10.1021/acs.jctc.6c01210 Read Online

ACCESS | Metrics & More | Article Recommendations | Supporting Information

ABSTRACT: Understanding how protein environments regulate the photodynamics of chromophores is a central task in quantum biology and remains a major challenge. This challenge is particularly significant for G protein-coupled receptors (GPCRs), which are natively nonphotochromic but can be optically controlled via synthetic photoswitchable ligands. Such artificial photoreceptors are new and important because they not only enable the photocontrol of signaling processes beyond those regulated by rhodopsins but also deepen our fundamental understanding of quantum effects in light-protein interactions. However, the ultrafast nonadiabatic dynamics of these ligands in GPCRs remain difficult to resolve experimentally, while traditional computational approaches fail to describe these processes accurately and efficiently. Here, we employed a multiscale framework to comprehensively characterize how receptor binding, mutations, receptor subtype, chemical substitution, and binding pocket electrostatics regulate the photodynamics of photoswitchable antagonists (OPs) of β-adrenergic receptors (β-ARs). This framework integrates extensive first-principles ground-state conformational sampling, absorption-spectra calculations, and nonadiabatic dynamics simulations. Chemical substitutions influence how excitation energy, excited-state lifetimes, and quantum yields (QY) respond to receptor binding, subtype changes, and binding-pocket mutations. The F289A and Y199A mutants generally accelerate excited-state dynamics by reducing local contacts, whereas the D113E mutation slows the dynamics of OP2 in β_2-AR by reducing the excited-state driving force. Neutralizing the charge of the counterion D113 residue via protonation increases the QY of OP2 in β_2-AR by altering the local electrostatic and hydrogen-bonding environment. The ultrafast photoisomerization of the ligands does not require large binding-pocket expansion. Overall, this work provides new insights into how binding-pocket environments regulate the photochemical properties of photoswitchable ligands targeting GPCRs.



INTRODUCTION

Photochemical reactions in proteins underlie many fundamental life processes, including vision, photosynthesis, circadian rhythms, and magnetoreception. These reactions often occur on femtosecond-to-picosecond time scales in multiple electronic states, where the dynamics of nuclear and electronic degrees of freedom are strongly coupled during nonadiabatic transitions.[1,2] These reactions exhibit strong quantum effects, meaning neither the energetics nor the dynamics can be described by molecular simulations using conventional classical mechanical methods.[1,2] In photoactive proteins, the surrounding protein environment often perturbs the photochemical reactivity of the chromophore through electrostatics, van der Waals, and hydrogen bond interactions. The excitation energies, excited-state lifetimes, reaction pathway, and quantum yields (QYs) can depend strongly on subtle changes in the protein environment.[1−9] This phenomenon has been well studied in rhodopsins, an important family of G protein-coupled receptors (GPCRs),[2,4,5,7−14] where the photochemical and photophysical properties of the retinal protonated Schiff base (RPSB) in the protein can differ significantly from those observed in solution, and among distinct subtypes and mutants.

Furthermore, protein control of chromophores' photochemistry is a general phenomenon in biological photoreceptors extending beyond rhodopsins. In photoactive yellow protein, chromophores in the aqueous solution and protein environment exhibit distinct excited-state decay kinetics, while mutations of the Pro68 residue can alter hydrogen bonding and hydration in

Received: June 17, 2026
Revised: September 8, 2026
Accepted: October 9, 2026

ACS Publications
© XXXX The Authors. Published by American Chemical Society

Downloaded from pubs.acs.org/jctcce/article-pdf/doi/10.1021/acs.jctc.6c01210/6902145/3/acs.jctc.6c01210.pdf by TEXAS TECH UNIV user on 29 October 2026

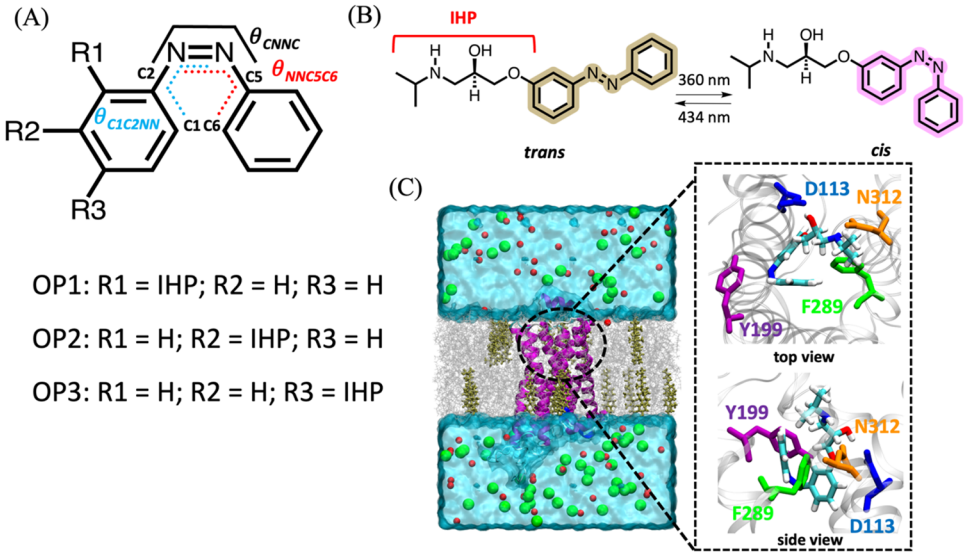


Figure 1. (A) Chemical structures of the OP photoswitches containing different substitutions. The side chain, 3-(isopropylamino)-2-hydroxypropoxy, is abbreviated as IHP. The IHP substituent is attached at different positions of the azobenzene moiety. (B) Schematic representation of the reversible photoisomerization of OP2 induced by illumination at different wavelengths. (C) Simulation setup of β_2-AR embedded in a mixed DOPC/cholesterol membrane environment. The ligand-binding pocket is illustrated using OP2 as an example. The selected residues, including D113, Y199, F289, and N312, are highlighted in the binding pocket, from both top and side views. Cholesterol molecules, Na^+, and Cl^- ions are shown in tan, red, and green, respectively. For clarity, water molecules and DOPC lipids are rendered transparent. The simulation setup of the β_1-AR is illustrated in Figure S1.

the chromophore binding pocket and reduce the photoisomerization quantum yield.[15,16] In the bacteriophytochromes RpBphP2 and RpBphP3, deletion of the PHY domain or perturbation of conserved hydrogen-bond networks elongates the chromophore's excited-state lifetime; in RpBphP3, these changes also increase fluorescence yield.[17] Studies on other phytochromes, such as DrBph and All2699g1, indicated that steric confinement and hydrogen bonding control the chromophore's excited-state decay kinetics and quantum yield.[18,19] Similarly, different active-site conformations and hydrogen bonding produce distinct FMN-quenching kinetics in the blue light using flavin (BLUF) domains.[20]

Recently, synthetic photoswitchable ligands have emerged as novel tools for reversible and precise photocontrol of cell signaling.[21−34] Through photoisomerization and thermal isomerization, some of these ligands can reversibly change their structure and binding affinity with the target GPCR, thereby switching their activity bidirectionally.[21−29] By targeting GPCRs that are not naturally photoactive, these photoswitchable ligands greatly expand the scope of biological processes that can be remotely regulated by light with high spatiotemporal resolution, opening new avenues for the mechanistic investigation of various signaling pathways. Also, by reversibly and precisely targeting GPCRs in a light-regulated and selective manner, these ligands are potential drug candidates that minimize the side effects associated with traditional chemotherapeutics. Beyond these applications, these photoswitch-enabled receptor systems are also highly tunable through ligand synthesis or receptor mutagenesis, thereby providing an ideal platform for mechanistic studies of how membrane receptors regulate the ultrafast photodynamics of small chromophores.[35−37] Among class A GPCRs, β-adrenergic receptors (β-ARs) are particularly important and well-studied because of their central roles in cardiovascular and respiratory physiology and as therapeutic targets.[21,25−29,38−40] Recently, a series of photoswitchable antagonists of β-ARs was developed based on propranolol,[22−24] a widely used β-blocker. Substitution of the naphthalene group on the propranolol with an azobenzene moiety produced a series of photoswitchable analogs, i.e., opto-prop-1 (OP1), opto-prop-2 (OP2), and opto-prop-3 (OP3)[22,24] (Figure 1A). Experimentally, these compounds exhibit substantial light-responsive binding affinity differential with their target[22] ($\Delta\Delta G_{\text{binding},cis\rightarrow trans}$), especially for OP2 with β_2-AR.[22,24] Indeed, these ligand−receptor systems, in particular the OP2 complexed with β_2-AR, represent one of the most successful examples of class A GPCR photopharmacology to date.[22,24] Several binding-pocket mutations, including Y199A, F289A, and D113E, alter the light-responsive affinity differential of the photoswitches.[24,41] These observations suggest that subtle changes in ligand substitution and binding-pocket environment could influence the ligand−receptor interactions. Although recent progress in time-resolved crystallography has captured a few snapshots of an individual photoswitchable ligand in the wild-type (WT) β_2-AR after nanoseconds to seconds of photoexcitation,[35] it remains largely unknown the general molecular mechanisms underlying the ultrafast photodynamics on the femtosecond to picosecond time scales, as well as the impact of protein mutation, receptor subtype, and chemical substitutions on the photochemical and photophysical properties. This is mainly due to the limitations in the spatiotemporal resolutions of experimental techniques for this new class of systems. Therefore, it is crucial for computational modeling to fill this gap and elucidate the photodynamics of these GPCR-ligand complexes exhibiting non-native photoactivity.

Molecular simulations of photodynamics in biomolecular environments require characterization of the coupled chromophore−protein system rather than isolated chromophores alone. This is especially important for understanding how mutations regulate the photodynamics of photoswitchable ligands in complex biomolecular environments. First-principles nonadiabatic dynamics simulations provide a powerful tool because they can directly propagate the coupled nuclear-electronic dynamics governing the excited-state relaxation at all-atom, all-electron resolution. However, accurately describing these

https://doi.org/10.1021/acs.jctc.6c01210
J. Chem. Theory Comput. XXXX, XXX, XXX−XXX

Downloaded from pubs.acs.org/jctcce/article-pdf/doi/10.1021/acs.jctc.6c01210/6902145/acs.jctc.6c01210.pdf by TEXAS TECH UNIV user on 29 October 2026

processes remains computationally demanding because it requires characterizing the potential energy surfaces of coupled electronic states and propagating the electronic and nuclear wave functions according to the time-dependent Schrödinger equation.[42,43] These requirements become even more challenging in biomolecular systems since one needs to accurately describe the influence of the protein environment on the excited- and ground-state energy surfaces and dynamics.[34,38,44,45] Local electrostatics, steric constraints, and conformational fluctuations in protein−ligand interactions could play important roles in determining the outcomes of photochemical reactions.[46−52] Consequently, nonadiabatic dynamics simulations performed in the quantum mechanics/molecular mechanics (QM/MM) setting are essential for understanding photochemical reactions in proteins at the atomistic level.[3,53]

To address these challenges, here, we employed a multiscale computational framework that combined ground-state MM and QM/MM sampling, absorption spectra calculation, and *ab initio* multiple spawning (AIMS).[54−56] Importantly, the AIMS simulations describe nonadiabatic dynamics by explicitly propagating coupled nuclear and electronic wave functions according to the time-dependent Schrödinger equation, providing a rigorous treatment of population transfer and electronic decoherence during photoisomerization. In this work, the AIMS simulations were coupled with on-the-fly electronic structure calculations using the hole−hole Tamm−Dancoff approximated density functional theory (hh-TDA-DFT) in a QM/MM setting to compute energies and nonadiabatic couplings among the ground- and excited states. This multiscale framework has been well-benchmarked in our previous studies of other photoactive protein systems,[3,53,57−63] and it enables systematic characterization of how mutations, receptor subtypes, chemical substitutions, and conformational fluctuations modulate the photodynamics of photoswitchable ligands in GPCRs.

Here, we comprehensively investigated the *cis*-to-*trans* photoisomerization of OPs in aqueous solution and in complex with WT β_1-AR, WT β_2-AR, the F289A, Y199A, and D113E mutants of β_2-AR. These simulations show that relatively small changes in ligand substitution, receptor subtype, binding-pocket mutations, and charge neutralization via protonation can alter the excitation energies, excited-state dynamics, and isomerization QYs.

COMPUTATIONAL METHODS

We employed a multiscale computational workflow integrating classical molecular dynamics (MD), ground-state QM/MM MD sampling, vertical excitation energy calculations, and *ab initio* multiple spawning (AIMS) simulations. Classical MD simulations were first performed to equilibrate the receptor−ligand complexes and the corresponding aqueous solution systems. Representative configurations of the system, sampled from these trajectories, were further refined using ground-state DFT/MM MD simulations to improve the description of the photoswitches in their surrounding environments, which is critical for absorption-spectrum calculations and nonadiabatic dynamics simulations. UV−vis absorption spectra were subsequently calculated from the configurations sampled from ground-state DFT/MM MD trajectories using the hh-TDA-DFT/MM method. Configurations were then selected from these ensembles to best represent the UV−vis spectra and used as initial conditions (ICs) for AIMS simulations, estimating the excited-state lifetime and *cis*-to-*trans* photoisomerization quantum yields (QYs). This computational framework was applied to OP1, OP2, and OP3 in the aqueous solution and in complex with β_1-AR and β_2-AR, as well as several β_2-AR mutants.

System Setup and MD Equilibration Simulations

The crystal structure of the inactive β_2-AR in complex with propranolol (PDB ID: 6PS5)[64] was used as the initial structure for the β_2-AR simulations, and the crystal structure of β_1-AR bound to carazolol (PDB ID: 7BVQ)[65] was used to prepare the β_1-AR systems. Consistent with previously reported simulation protocols,[66] the fused T4-lysozyme (T4L) domain present in the crystal structure of β_2-AR was removed prior to system preparation. The missing intracellular loop 3 (ICL3) region was reconstructed as a flexible, unstructured loop using the MODELLER package.[67] In addition, mutated residues in the crystal structure were reverted to the WT ones during this process (Figure 1C). The F289A, Y199A, and D113E single-point mutations were also introduced during this process. The crystallized propranolol molecule was removed, and molecular docking simulations were performed with AutoDock Vina[68] to position a single OP molecule within the receptor binding cavity in the *cis* isomer. The resulting binding poses were visually inspected to ensure that the azobenzene scaffold and the IHP side chain properly maximally overlapped with the aromatic ring and the IHP side chain of the propranolol in the crystal structure.[22] In addition, the ligand binding poses were compared with the docking poses previously reported by Shi et al.[24] This visual inspection step is important for preserving specific protein−ligand interactions in the parent compound (propranolol) and for analyzing the effects of binding-pocket mutations.

Protonation states of all ionizable residues at neutral pH were assigned using the H++ web server,[69] except for D113, for which both protonated and deprotonated states were simulated to assess the effects of changes in protonation and charge state in the binding pocket on the photoisomerization.[69] The membrane-protein systems were generated using the CHARMM-GUI.[70] Both receptors were inserted into lipid bilayers capped by water molecules on each side (Figures 1C and S1). The membrane composition consisted of 180 DOPC (1,2-dioleoyl-*sn*-glycero-3-phosphocholine) lipids and 10 wt % cholesterol. This lipid composition was selected based on previous studies showing the influence of cholesterol concentration on receptor stability and membrane dynamics.[71,72] To reproduce physiological ionic conditions, NaCl was added to a final concentration of 0.15 M, which also neutralized the total charge of each simulation system. The final periodic boundary condition (PBC) simulation boxes had dimensions of ∼100 × 100 × 140 Å^3 for the β_2-AR systems (Figure 1C) and ∼100 × 100 × 170 Å^3 for the β_1-AR systems (Figure S1), with PBC applied in all directions.

The solvent environment was modeled using the TIP3P water model,[73] and the FF14SB[74] and LIPID17[75] force fields were applied to the protein and membrane, respectively. Parameters for OP1, OP2, and OP3 were obtained using the General AMBER Force Field (GAFF).[76,77] Because the photoisomerization of azobenzene derivatives is highly sensitive to rotational flexibility around the azo group, additional force field refinement was performed for the three key dihedrals of the azobenzene unit. In particular, the C2−N3 = N4−C5 (θ_{CNNC}), C1−C2−N3 = N4 (θ_{C1C2NN}), and N3 = N4−C5−C6 (θ_{NNC5C6}) dihedral angles (Figure 1A) were reparametrized using relaxed quantum mechanical (QM) potential energy surface (PES) scans. This

Downloaded from pubs.acs.org/jctcce/article-pdf/doi/10.1021/acs.jctc.6c01210/6902145/3/acs.jctc.6c01210.pdf by TEXAS TECH UNIV user on 29 October 2026

https://doi.org/10.1021/acs.jctc.6c01210
J. Chem. Theory Comput. XXXX, XXX, XXX−XXX

refinement step was necessary because our previous study[57] showed that the default GAFF torsional terms have artificially low barriers, leading to facile thermal *cis* ↔ *trans* isomerizations during MD simulations. As a result, refinement of these dihedral parameters was required to faithfully sample the representative ground-state conformational ensemble of the *cis* isomers of the photoswitches, based on which absorption spectra and nonadiabatic dynamics simulations can be performed accurately. The QM calculations used for the torsional parameter optimization employed the hh-TDA-DFT approach[58] with the BH&HLYP functional and the 6−311++G(d,p) basis set.[61] This first-principles multireference method incorporates both static and dynamic electron correlation, and has been extensively validated for describing the photo- and thermal isomerization of azobenzene-based photoswitches.[3,53,57−62] A more detailed description of the torsional refinement workflow for these compounds was reported in our recent study.[41] All QM calculations for force-field parametrization were carried out using the TeraChem software package.[78,79]

In the MD simulations, each system was subjected to 100,000 steps of energy minimization to eliminate unfavorable contacts. The system was then equilibrated in the constant NVT ensemble at 300 K for 5 ns using a 1 fs time step. During this step, positional restraints of 5.0 kcal/mol/Å^2 were applied to the protein heavy atoms. This initial equilibration step was followed by a 50 ns equilibration in the constant NPT ensemble at 300 K and 1 bar, where the positional restraints were gradually reduced and eventually removed. Production simulations were then performed for 200 ns in the same constant NPT ensemble with a time step of 2 fs and no restraints. The pressure was controlled using the Berendsen barostat[80] with a relaxation time constant of 1 ps, using isotropic coupling for ligands in aqueous solution and anisotropic coupling for membrane-receptor systems. The temperature was controlled using a Langevin thermostat[81] employing a friction coefficient of 1 ps^{-1}. Electrostatic interactions were evaluated using the Particle Mesh Ewald (PME) method,[82] and van der Waals interactions were treated with a cutoff distance of 12 Å. All covalent bonds involving hydrogen atoms were constrained with the SHAKE algorithm throughout the simulations.[83]

In addition to the receptor-bound systems, all OP ligands were also simulated in aqueous solution. For these calculations, each ligand was solvated in a PBC box containing water molecules with dimensions of ∼50 × 50 × 50 Å^3, followed by the same energy minimization, equilibration, and production MD simulation procedures described above. All MD simulations were conducted using the AMBER24 simulation package.[84]

Ground-State QM/MM MD Equilibration

Additional ground-state sampling is necessary to correct the inaccuracies in the force field descriptions of ligand bond lengths and torsional coordinates, which could significantly affect the subsequent absorption spectra and nonadiabatic dynamics. Thus, after the classical MD simulations, ground-state DFT/MM MD simulations were carried out to refine the sampling of ligand structures. Since the ground-state PES of DFT/MM near the Franck−Condon (FC) region is very similar to that of hh-TDA-DFT/MM, this additional sampling step ensures maximal compatibility with subsequent spectral and nonadiabatic dynamics simulations using hh-TDA-DFT/MM.

For each system, 50 configurations were then selected from the final 100 ns of the classical MD trajectory at 2 ns intervals. For each selected configuration, an open-boundary subsystem was constructed from the original PBC simulation box. To construct this subsystem, water molecules and ions were selected only if they contained at least one atom within 10 Å of any protein atom in the full PBC system. The retained ions were taken directly from the equilibrated MD snapshots, and no additional ions were introduced to neutralize the net charge of the system after truncation to avoid perturbing the equilibrated local solvation structure and electrostatic environment near the surfaces of the protein and lipid bilayer. Applying the same protocol to construct all ICs across all systems, the initial condition (IC) sampling can, to some extent, average out the net charge effects within each system. Error cancellation further mitigates these effects when analyzing trends across systems.

This system truncation was required because the version of the TeraChem package[78,79,85,86] used in this study did not support full PBC for on-the-fly hh-TDA-DFT/MM calculations during the nonadiabatic dynamics simulations.

In the QM/MM MD calculations, the QM region included only the ligand and was described using the BH&HLYP functional and the 6−31G* basis set.[87] All remaining components of the system were treated at the MM level using the force fields described above. This QM/MM setup follows the strategy used in our previous study of protein−ligand effects on the ground-state isomerization kinetics of photostatins,[61] as well as related computational studies of photoactive molecular systems.[3,57,63,88] Electrostatic embedding was used, i.e., the electronic structure of the QM region was evaluated in the electrostatic field generated by the fixed-point charges of the MM environment. Each ground-state QM/MM MD trajectory was propagated for 2 ps in the constant NVT ensemble at 300 K using a 0.5 fs time step. The temperature was controlled with a Langevin thermostat.[85] The same QM/MM equilibration protocol was also applied to the *cis* isomer of all OP compounds in aqueous solution. All ground-state QM/MM MD simulations were performed using TeraChem[78,79,85,86] interfaced with the OpenMM packages.[89]

Absorption Spectra Calculations

To generate the absorption spectra of the OP photoswitches, configurations were sampled from the ground-state QM/MM MD trajectories obtained for both the receptor-bound and aqueous environments. Specifically, snapshots were extracted every 10 fs over the 2 ps QM/MM equilibration trajectories generated from each of the 50 initial configurations, resulting in a total ensemble of 10,000 geometries for every ligand in both the bound and unbound states. For each sampled geometry, vertical excitation calculations were performed using the hh-TDA-BH&HLYP/6−31G*/MM method, with the same QM/MM partitioning and electrostatic embedding scheme as described above. The excitation energies and the corresponding oscillator strengths associated with the $S_0 \rightarrow S_1$ transition were collected from all calculations and then used to construct the absorption spectra following the protocol described in ref 90. Specifically, Lorentzian functions with an FWHM of 0.05 eV were used to convolve the discrete data points of excitation energies and oscillator strengths. This broadening width was selected after testing FWHM values from 0.01 to 0.05 eV and is also within the range commonly used in absorption spectra calculations.[91,92] Broadening with Gaussian functions of the same FWHM yielded nearly identical excitation energies and the same overall spectral trends (Table S1), indicating that the results are not sensitive to the choice between Lorentzian and Gaussian functions.

Downloaded from pubs.acs.org/jctcce/article-pdf/doi/10.1021/acs.jctc.6c01210/6902145/3/acs.jctc.6c01210.pdf by TEXAS TECH UNIV user on 29 October 2026

https://doi.org/10.1021/acs.jctc.6c01210
J. Chem. Theory Comput. XXXX, XXX, XXX−XXX

AIMS Simulations. The ICs used for the AIMS simulations were selected from the ground-state QM/MM MD trajectories of the OP photoswitches in both the receptor-bound and aqueous solution systems. The coordinates and velocities obtained from the QM/MM MD trajectory were used as ICs for AIMS simulations. To construct a reduced but statistically representative ensemble for the excited-state dynamics simulations, the complete set of 10,000 QM/MM MD geometries was subsampled to best reproduce the absorption spectra calculated from the full ensemble with 50 snapshots. The validity of this reduction procedure was confirmed by comparing the absorption spectrum reconstructed from the 50 selected ICs with that obtained from the full 10,000 frames, as shown in Figure S2 for all OPs in aqueous solution as an example.

For each system, 50 independent ICs were used to initiate the AIMS simulations by placing the system in the first singlet excited state (S_1). The lowest three singlet states, i.e., the S_0 to S_2 states, were included in the AIMS simulation. The full multiple spawning (FMS) algorithm was employed to propagate the coupled nuclear and electronic wave functions. Specifically, the evolving nuclear wave function is expanded in terms of trajectory basis functions (TBFs) propagated on multiple electronic states. Each TBF is a multidimensional frozen-width Gaussian nuclear basis function associated with a particular electronic state. The centroid of each TBF corresponds to the atomic coordinates of the entire QM/MM system. The amplitudes and centroids of the TBFs evolved together according to the time-dependent Schrödinger equation using the FMS algorithm. Population transfer between electronic states naturally arises from new TBF spawning and amplitude transfer among the TBFs. Briefly, when a TBF traveling on one electronic state enters a region of strong nonadiabatic coupling with another state, a new TBF is generated on the other state. During this process, a portion of the original TBF amplitude is transferred to the newly created TBF, thereby enabling population transfer between electronic states. After a nonadiabatic transition, if the TBFs in different states experience different forces, they move apart and become decoupled, which naturally leads to the decoherence in the dynamics of their amplitudes.[56] This feature represents a major advantage of the FMS algorithm over conventional Ehrenfest and surface-hopping methods, which need decoherence corrections.[54]

All on-the-fly electronic structure calculations, including energies, nuclear gradients, and nonadiabatic coupling vectors, were evaluated using the hh-TDA-BH&HLYP/6−31G*/MM method within the QM/MM setting described above. The three lowest singlet electronic states (S_0, S_1, and S_2) were explicitly included in the AIMS simulations. Different integration timesteps were employed depending on the strength of the nonadiabatic coupling. A time step of 20 au was used in regions of PES with weak nonadiabatic coupling, whereas a reduced time step of 5 au was applied whenever the system entered strongly coupled regions of the PES, triggering spawning events. The simulations were propagated until more than 95% of the excited-state population had relaxed to the ground electronic state. The AIMS simulations were performed with the FMS90 code interfaced with the TeraChem/OpenMM packages.

The excited-state lifetime of each system was characterized by analyzing the time evolution of the S_1 population obtained from the AIMS trajectories. The population decay profile, $P_{S_1}(t)$, was fitted using a first-order kinetics model (eq 1)

$$P_{S_1}(t) = \exp\left(-\frac{t}{\tau}\right) \quad (1)$$

where t denotes the time after photoexcitation and τ corresponds to the excited-state decay time constant associated with relaxation back to the ground state. The evolution of the S_1 state population does not exhibit a clear plateau before the onset of the decay. We therefore found no evidence for a distinct induction period, did not introduce an initial delay time constant term in the fitting, and instead used a single exponential function.

The isomerization QY was determined from the final ground-state population distribution obtained at the end of the AIMS simulations. A trajectory was considered to form the *trans* photoproduct when the absolute value of the final azobenzene dihedral angle was greater than 90 degrees, i.e., $|\theta_{CNNC}| > 90°$, where $-180° < \theta_{CNNC} < 180°$. The isomerization QY was then calculated as the fraction of the total ground-state population that ended in the *trans* isomer, relative to the total population of ground-state TBFs at the end of the AIMS simulation. To quantify statistical uncertainties in properties derived from AIMS simulations, the bootstrapping analysis was performed using 1000 samples drawn from the 50 ICs. To assess convergence of the AIMS simulation results with respect to the number of ICs used, the time evolutions of the S_1 population were recalculated using randomly selected sets of 10, 20, 30, 40, and 50 ICs for OPs in aqueous solution, β_1-AR, and β_2-AR. The fitted decay time constants gradually converge as the number of ICs increases, with the results from 40 and 50 ICs agreeing within their statistical uncertainties for all systems examined (Figure S3 and Table S2).

RESULTS

The simulations we performed were designed to determine how chemical substitutions, receptor subtypes, binding-pocket mutations, and counterion charge neutralization regulate the ultrafast *cis*-to-*trans* photoisomerization of OPs in β-ARs. We examined OP1, OP2, and OP3 in aqueous solution and in the wild-type (WT) β_2-AR, β_1-AR, and selected β_2-AR mutants. Since the photoswitchable inhibition of β_2-AR by OP2 represents one of the most successful examples of class A GPCR photopharmacology with extensive mutagenesis data,[22,24] the photodynamics of OP2 was investigated in additional β_2-AR variants (such as the D113E mutant and the WT with a protonated D113 residue). In total, 17 systems were investigated. For each system, 50 ICs were selected from ground-state QM/MM MD simulations for AIMS simulations, and absorption spectra were calculated from 10,000 QM/MM geometries. The accuracy of the hh-TDA-BH&HLYP method extensively employed in the spectra and nonadiabatic dynamics simulations was benchmarked against the XMS-CASPT2 method, with results summarized in the SI section "Benchmark Calculations" and Table S5.

Absorption Spectra

The calculated spectra show that all OPs can be photoexcited through the $S_0 \rightarrow S_1$ transition, which is dominated by the $n\pi^*$ excitation (Figure S4 and Table S1). Thus, the receptor environment does not fundamentally change the identity of the initially excited state. For OP2 in aqueous solution, the S_1 and S_2 contributions form clearly separated absorption bands (Figure S4). The average oscillator strength of the $S_0 \rightarrow S_1$ transition is 0.27 ± 0.08, compared with 0.14 ± 0.06 for $S_0 \rightarrow S_2$.

Downloaded from pubs.acs.org/jctcce/article-pdf/doi/10.1021/acs.jctc.6c01210/6902145/3/acs.jctc.6c01210.pdf by TEXAS TECH UNIV user on 29 October 2026

https://doi.org/10.1021/acs.jctc.6c01210
J. Chem. Theory Comput. XXXX, XXX, XXX−XXX

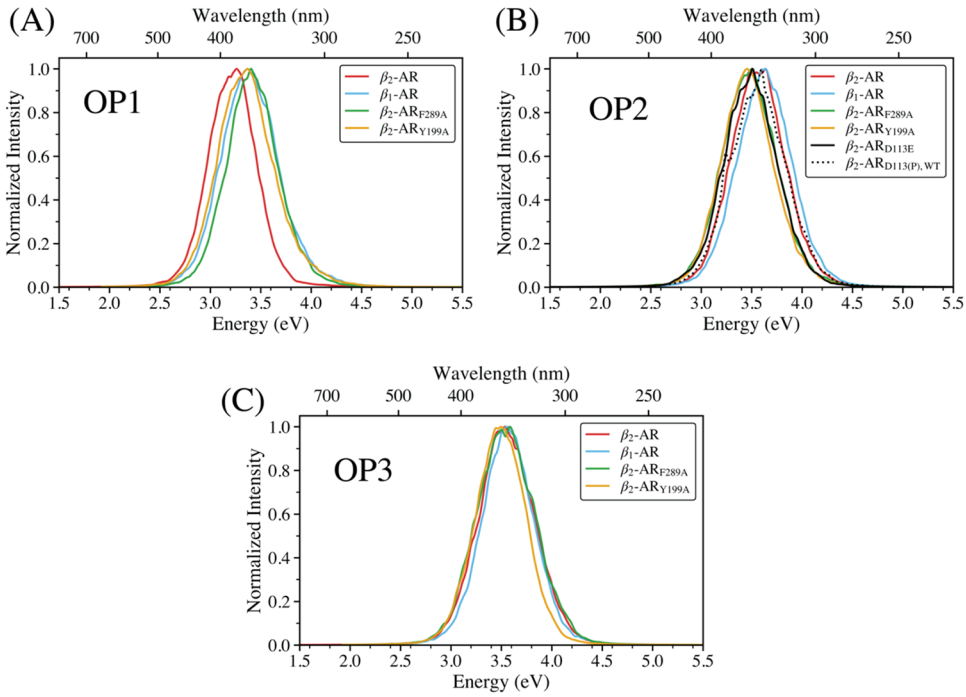


Figure 2. Calculated UV−vis absorption spectra for the $S_0 \rightarrow S_1$ ($n\pi^*$) excitation of OP photoswitches in complex with WT β_1-AR, WT β_2-AR, and β_2-AR mutants. (A) Comparison of the calculated absorption spectra of OP1 in the WT β_1-AR, WT β_2-AR, β_2-AR$_{F289A}$, and β_2-AR$_{Y199A}$. (B) Calculated absorption spectra of OP2 in the WT β_1-AR, WT β_2-AR, β_2-AR$_{F289A}$, β_2-AR$_{Y199A}$, and β_2-AR$_{D113E}$, and the WT β_2-AR with a protonated D113 residue (β_2-AR$_{D113(P),WT}$). (C) Calculated absorption spectra of OP3 in β_1-AR, β_2-AR, β_2-AR$_{F289A}$, and β_2-ARY$_{199A}$. Table S1 reports the maximal absorption excitation energies for all systems.

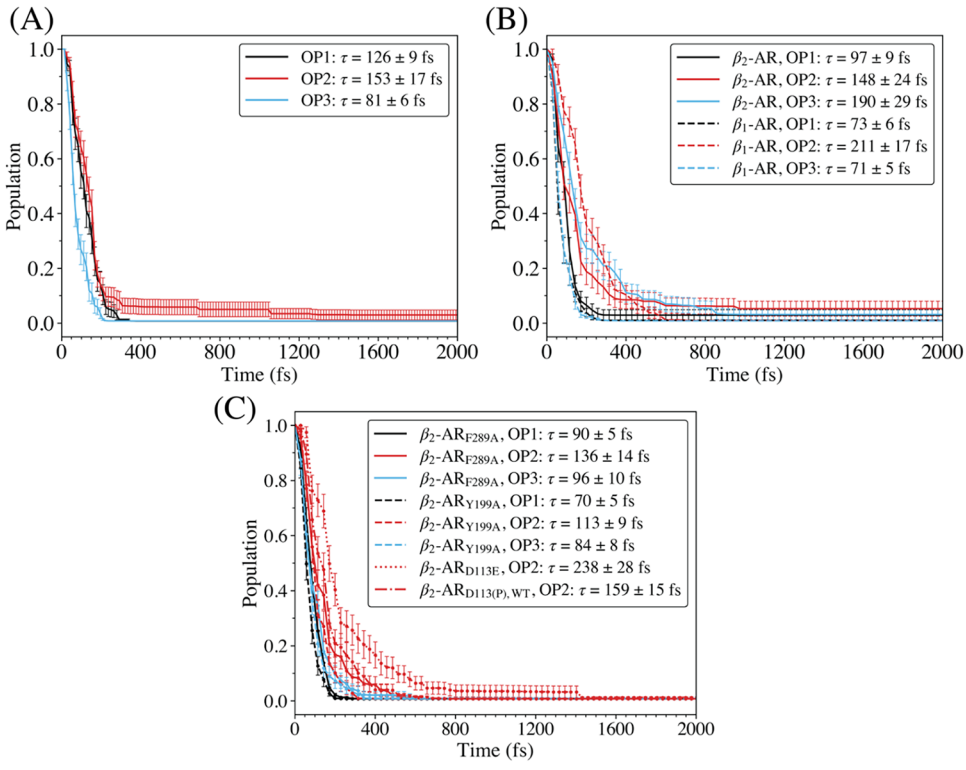


Figure 3. Time evolution of the S_1 excited-state population during the *cis*-to-*trans* photoisomerization following $S_0 \rightarrow S_1$ photoexcitation of the OPs in the aqueous solution and the WT β_1-AR, WT β_2-AR, and β_2-AR mutants, obtained from AIMS simulations. (A) OPs in the aqueous solution. (B) OPs in the WT β_1-AR and WT β_2-AR. (C) OPs in the mutants of β_2-AR and WT β_2-AR with a protonated D113 residue.

Thus, despite its predominant $n\pi^*$ character, the S_1 transition has a considerable oscillator strength and remains directly accessible by photoexcitation. Furthermore, in the experimental study of the OPs,[22] the excitation wavelength ranges from 420 to

https://doi.org/10.1021/acs.jctc.6c01210
J. Chem. Theory Comput. XXXX, XXX, XXX−XXX

Downloaded from pubs.acs.org/jctcce/article-pdf/doi/10.1021/acs.jctc.6c01210/6902145/acs.jctc.6c01210.pdf by TEXAS TECH UNIV user on 29 October 2026

430 nm, corresponding to the $S_0 \rightarrow S_1$ ($n\pi^*$) excitation peak of azobenzene derivatives. This is the main reason we selected the S_1 ($n\pi^*$) state as the initial state for the AIMS simulations.

The clearest substituent effect on the spectra is observed in aqueous solution (Figure S5). OP1 has the lowest S_1 excitation energy, with an absorption maximum at 3.46 eV, whereas OP2 and OP3 absorb at higher and nearly identical energies of 3.65 and 3.58 eV, respectively (Table S1). Thus, OP1 is red-shifted relative to OP2 and OP3 by approximately 0.12−0.19 eV. Receptor-binding generally red-shifts the spectra of the OPs, especially for OP1. For example, OP1's spectrum in β_2-AR is red-shifted relative to aqueous solution by approximately ∼0.20 eV. Mutations can also significantly shift the spectra (Figure 2 and Table S1). For example, relative to the WT β_2-AR, the F289A mutant blue-shifts OP1's absorption spectrum by ∼0.15 eV, whereas the Y199A mutant red-shifts OP2's spectrum by ∼0.18 eV. Charge neutralization of the D113 residue via protonation results in minimal shifts in the absorption spectra of the OP2 in WT β_2-AR (Figure 2B).

The small differences in the maximum absorption excitation energies of these systems indicate that, under the wavelength that promotes $S_0 \rightarrow S_1$ $n\pi^*$ excitation in aqueous solution, the OPs in the receptors also predominantly undergo the same excitation, justifying our choice to initiate the AIMS simulations of all systems in the S_1 state. Thus, the main photochemical differences among the OP systems arise not from a qualitative change in the excited state but from differences in excited-state dynamics and nonadiabatic relaxation after photoexcitation. As discussed below, receptor binding, receptor subtype, binding-pocket mutations, and charge perturbations primarily affect the subsequent excited-state dynamics, the nonadiabatic transition, and the ground-state branching ratio between the *cis*-isomer reactant and *trans*-isomer products.

Coupled Effects of Substituents and Receptor Binding on Photodynamics

The comparison of the S_1-state lifetime (τ) and *cis*-to-*trans* photoisomerization QYs of OPs in the aqueous solution and WT β_2-AR reveals the coupled effects of chemical substitutions and receptor binding. In aqueous solution, the three OPs have distinct τ and QYs (Figure 3A and Table 1), demonstrating substituent effects on the photodynamics. OP3 has the fastest nonradiative decay, with τ = 81 ± 6 fs, whereas OP1 and OP2 decay more slowly, with τ = 126 ± 9 fs and 153 ± 17 fs, respectively. However, this trend in τ is not correlated with the trend in their QY. OP1 has the highest QY, 56 ± 5%, OP2 has an intermediate QY, 47 ± 5%, and OP3 has the lowest QY, 41 ± 5%. The difference in the QYs of OP1 and OP3 is beyond statistical uncertainty. Therefore, in the aqueous solution, faster excited-state decay does not necessarily lead to higher quantum efficiency of *cis*-to-*trans* photoisomerization.

Binding to WT β_2-AR affects the photodynamics in a ligand-specific manner (Figure 3B and Table 1). For OP1, receptor binding shortens the τ from 126 ± 9 fs in the aqueous solution to 97 ± 9 fs but only slightly decreases the QY from 56 ± 5% to 53 ± 5%. For OP2, receptor binding slightly reduces τ from 153 ± 17 fs to 148 ± 24 fs, and decreases the QY from 47 ± 5% to 43 ± 5%. OP3 shows the opposite kinetic response: its τ increases from 81 ± 6 fs in the aqueous solution to 190 ± 29 fs in WT β_2-AR, while its QY increases from 41 ± 5% to 47 ± 5%.

These comparisons establish the first major finding of this study: chemical substitution controls how the OPs' photodynamics respond to receptor binding. The substituent effect is not restricted to spectra and photodynamics in aqueous solution. It also determines how receptor binding changes the excited-state dynamics, nonadiabatic relaxations, and photoproduct formation on the ground state. However, the QYs of the aqueous and receptor-bound systems remain comparable within their reported uncertainties. Therefore, the clearest ligand-dependent effect of receptor binding in these systems is observed in the excited-state relaxation kinetics rather than in the photoisomerization QY.

Table 1. Calculated S_1-State Lifetime (τ, in fs) and *cis*-to-*trans* Photoisomerization Quantum Yields (QY, %) of the OP Photoswitches in Aqueous Solution, WT β_2-AR, WT β_1-AR, and β_2-AR Mutants, Including F289A, Y199A, and D113E[a]

	OP1	OP2	OP3
	τ (fs)		
Aqueous solution	126 ± 9	153 ± 17	81 ± 6
β_2-AR	97 ± 9	148 ± 24	190 ± 29
β_1-AR	73 ± 6	211 ± 17	71 ± 5
β_2-AR$_{F289A}$	90 ± 5	136 ± 14	96 ± 10
β_2-AR$_{Y199A}$	70 ± 5	113 ± 9	84 ± 8
β_2-AR$_{D113E}$	N/A	238 ± 28	N/A
β_2-AR$_{D113(P),WT}$	N/A	159 ± 15	N/A
	QY (%)		
Aqueous solution	56 ± 5	47 ± 5	41 ± 5
β_2-AR	53 ± 5	43 ± 5	47 ± 5
β_1-AR	45 ± 5	43 ± 5	50 ± 6
β_2-AR$_{F289A}$	47 ± 5	46 ± 5	45 ± 5
β_2-AR$_{Y199A}$	58 ± 5	47 ± 5	44 ± 5
β_2-AR$_{D113E}$	N/A	46 ± 5	N/A
β_2-AR$_{D113(P),WT}$	N/A	55 ± 5	N/A

[a]The result of WT β_2-AR with a protonated D113 residue is also included (labeled as β_2-AR$_{D113(P),WT}$).

Coupled Effects of Substituents and Receptor Subtypes on Photodynamics

Comparing the excited-state lifetimes and QYs of OPs between WT β_1-AR and β_2-AR enables analysis of the effects of receptor subtype on photodynamics (Figure 3B and Table 1). Among the three OPs, OP1's photodynamics is most sensitive to the receptor subtype in terms of both relaxation time and quantum yield. Switching from β_2-AR to β_1-AR decreases the τ from 97 ± 9 fs to 73 ± 6 fs and reduces the QY from 53 ± 5% to 45 ± 5%. For OP2 and OP3, subtype switching affects excited-state kinetics but not the QY. For OP2, switching from β_2-AR to β_1-AR increases the τ from 148 ± 24 fs to 211 ± 17 fs, while the QY remains unchanged (43 ± 5%). For OP3, switching from β_2-AR to β_1-AR substantially decreases the τ from 190 ± 29 fs to 71 ± 5 fs, while the QY changes only modestly, from 47 ± 5% to 50 ± 6%.

The receptor subtype comparison establishes the second major finding: the distinct protein environments of β_1-AR and β_2-AR have nontrivial effects on the excited-state dynamics and nonadiabatic transition leading to photoisomerization, and such effects are ligand-dependent. The photodynamics of OP1 is the most sensitive to the choice of receptor subtype, whereas OP2 and OP3 show large changes in excited-state lifetimes but only modest changes in QYs. β_1-AR accelerates the excited-state relaxation of OP1 and OP3 relative to β_2-AR but slows that of OP2.

Downloaded from pubs.acs.org/jctcce/article-pdf/doi/10.1021/acs.jctc.6c01210/6902145/3/acs.jctc.6c01210.pdf by TEXAS TECH UNIV user on 29 October 2026

https://doi.org/10.1021/acs.jctc.6c01210
J. Chem. Theory Comput. XXXX, XXX, XXX−XXX

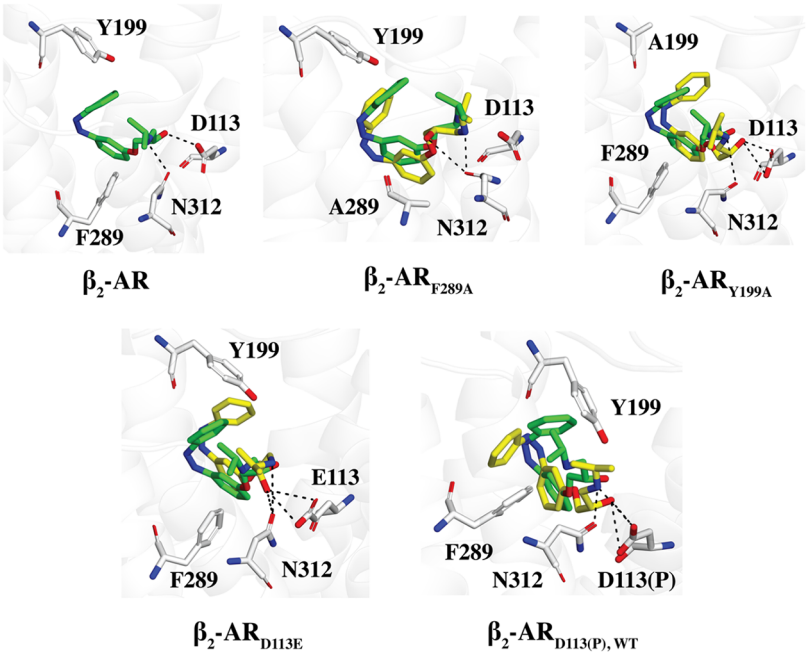


Figure 4. Comparison of representative OP2 binding poses for the WT β_2-AR with deprotonated D113 and the F289A, Y199A, and D113E mutants, as well as the WT β_2-AR with protonated D113. In the mutant structures, the OP2 binding pose in WT β_2-AR is shown in green, and OP2 in the mutant is shown in yellow to highlight changes in the ligand position within the binding pocket upon mutation. The nearby residues are shown in white, and hydrogen-bonding interactions are indicated by black dashed lines. β_2-AR denotes WT β_2-AR with deprotonated D113, whereas β_2-AR$_{D113(P),WT}$ denotes the same WT β_2-AR with protonated D113.

Effects of Binding-Pocket Mutations on Photodynamics

Mutations in the binding pocket of β_2-AR alter the excited-state relaxation kinetics and isomerization QY. After the MD simulations, *cis*-OP2 adopted a binding mode consistent with the docking calculation reported by Shi et al.[24] Its hydroxyl-containing side chain was anchored through polar interactions with D113 and N312 (Figure 4), while its azobenzene moiety formed contacts with the hydrophobic residues F289 and Y199. This combination of polar and hydrophobic interactions stabilized *cis*-OP2 within the binding pocket, in good agreement with a previous docking calculation.[24] The D113E, Y199A, and F289A mutations perturb these interactions, thereby altering the photodynamics of the ligands.

For OP1, both the F289A and Y199A mutations accelerate the decay of the S_1-state population relative to WT β_2-AR (Figure 3C and Table 1). The τ decreases from 97 ± 9 fs in the WT to 90 ± 5 fs and 70 ± 5 fs in the F289A and Y199A mutants, respectively. The QY decreases from 53 ± 5% in the WT to 47 ± 5% in the F289A mutant and increases to 58 ± 5% in the Y199A mutant. Thus, OP1 in Y199A is a case where faster S_1 decay is associated with higher QY.

For OP2, the F289A and Y199A mutants decrease the τ of the WT from 148 ± 24 fs to 136 ± 14 fs and 113 ± 9 fs, respectively, whereas the D113E mutant significantly elongates it to 238 ± 28 fs, the longest lifetime among all systems examined (Figure 3C and Table 1). However, none of the three mutations significantly changes the 43 ± 5% QY in the WT: 46 ± 5% for F289A, 47 ± 5% for Y199A, and 46 ± 5% for D113E. Although the S_1-state lifetime is much longer in D113E than in WT, it does not significantly affect the QY. The unusually slow S_1-state dynamics in D113E is analyzed in detail below from an energetic perspective, which shows that this mutation substantially reduces the energetic driving force from the FC region toward the vicinity of the S_1/S_0 conical intersection (CI) seam.

For OP3, F289A and Y199A both accelerate S_1 decay relative to the WT. The τ decreases from 190 ± 29 fs in the WT to 96 ± 10 fs in F289A and 84 ± 8 fs in Y199A (Figure 3C and Table 1). However, neither mutation perturbs the 47 ± 5% QY in the WT: 45 ± 5% in F289A and 44 ± 5% in Y199A.

The mutation results establish the third major finding: local binding-pocket mutations can alter the excited-state dynamics, but only modestly perturb the QY. The F289A and Y199A generally accelerate the excited-state dynamics for all three OPs, but their impact on the QY is modest and ligand-dependent. The D113E greatly slows the OP2's excited-state decay but does not significantly perturb the QY.

Effects of Counterion Charge Neutralization on the Photodynamics

In our discussions above, the D113 residue is treated as deprotonated, carrying one negative charge on the carboxyl group of its side chain, which forms a tight hydrogen bond with the IHP side chain of the OPs (Figure 4A). This deprotonated state was predicted by pK_a calculations using the H++ server. This residue is analogous to the anion counterions near the positively charged NH group of the RPSB in rhodopsins. In rhodopsins, perturbations in the charge state of the counterions near the RPSB chromophore have been shown to significantly modulate the character mixing of the excited states, the excitation energies, the excited-state potential energy surfaces, the reaction intermediates, the kinetics of nonadiabatic relaxation, and the fluorescence and isomerization quantum yields.[2,4,8,14,93,94] Due to the similarity of D113 to the counterions in rhodopsin, it is important to understand how perturbations in its protonation/charge state influence the photodynamics of the OPs.

Here, we used OP2 in β_2-AR as an example to investigate the effect of the D113 counterion residue on photodynamics. Our calculated results (Table 1) indicate noticeable effect of

https://doi.org/10.1021/acs.jctc.6c01210
J. Chem. Theory Comput. XXXX, XXX, XXX−XXX

Downloaded from pubs.acs.org/jctcce/article-pdf/doi/10.1021/acs.jctc.6c01210/6902145/acs.jctc.6c01210.pdf by TEXAS TECH UNIV user on 29 October 2026

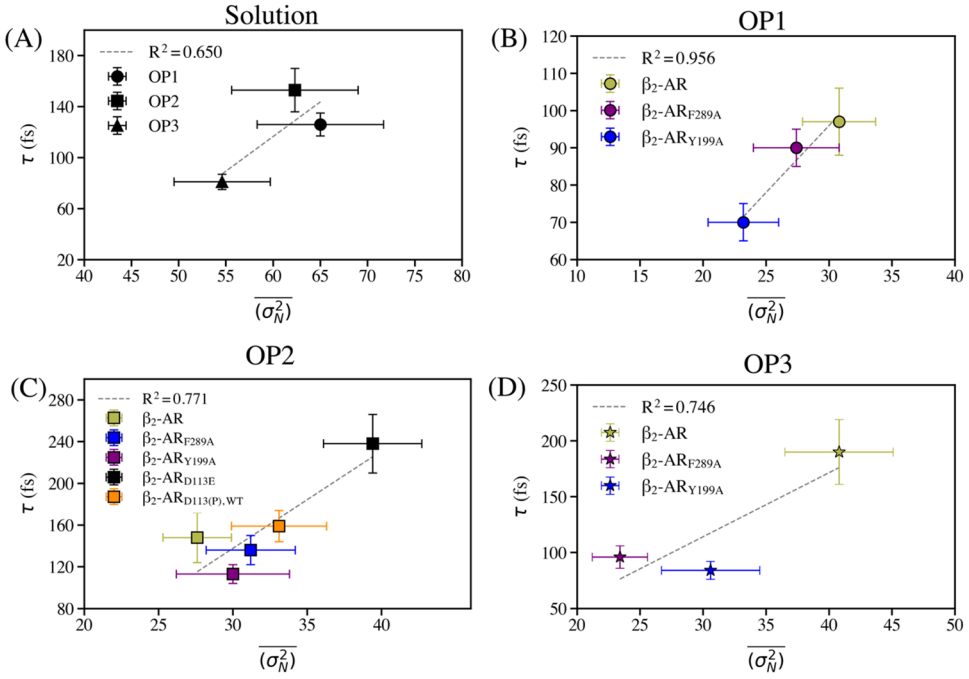


Figure 5. Relationship between the excited-state decay time constants (τ) and the average variance of the contact numbers $\left(\overline{\sigma_N^2}\right)$. (A) OP1, OP2, OP3 in aqueous solution, (B) OP1 in WT β_2-AR and its mutants, (C) OP2 in WT β_2-AR and its mutants, (D) OP3 in WT β_2-AR and its mutants.

protonating the D113 residue on photodynamics. Although the τ increases slightly from 148 ± 24 fs to 159 ± 15 fs upon protonation of D113, the QY increases significantly from 43 ± 5% to 55 ± 5%. The increase in QY indicates that neutralizing the counterion charge has non-negligible effects, even though the D113 residue does not directly interact with the azobenzene moiety. This may be due to the large shift in the position of the IHP side chain (Figure 4 and Figure S6) relative to the crystal structure of propranolol and OP2 in D113-deprotonated WT β_2-AR, as well as the change in the position of the azobenzene moiety. D113 protonation disrupts the crucial local hydrogen-bond network between the ligand's IHP side chain and the binding pocket, altering the ligand's interactions with surrounding residues and thereby affecting its QY. This analysis highlights another major finding of this study: strong perturbations in the electrostatics of the binding-pocket residues can influence the quantum efficiency of photoisomerization.

Distribution of $S_1 \rightarrow S_0$ Spawning Times

The S_1-state lifetimes reported in Table 1 were averaged across all ICs for each system. To directly examine how the nonadiabatic transition events are distributed in time among the AIMS trajectories, we compared the distributions of $S_1 \rightarrow S_0$ spawning times (Figure S7). The spawning-time distributions differ among the various ligands and receptor environments. In aqueous solution, the spawning events of OP3 are concentrated mainly at early times, consistent with its shorter S_1-state lifetime. The spawning times of OP1 and OP2 exhibit broader distributions, with larger contributions from later spawning events. In the receptor-bound systems, OP1 and OP3 in β_1-AR also show distributions dominated by early spawning events, whereas OP2 in β_1-AR has a broader distribution extending to later times. For the F289A and Y199A mutants of β_2-AR, most of the spawning events for OP1 and OP3 occur within the first 100 fs. In contrast, for the OP2 systems, the distributions are broader. For OP2 in the D113E mutant, there is a considerable contribution from spawning events beyond 150 fs, consistent with its longest S_1-state lifetime. Therefore, the spawning events are not distributed within the same narrow time range in all systems. Some systems have relatively compact distributions dominated by early events, whereas others show broader distributions with substantial late-time contributions. This analysis complements the analysis of the ensemble-averaged rate constants and indicates that the temporal distribution of the nonadiabatic transition events depends on both the ligand and its environment.

Effects of the S_2 State on the Photodynamics

To examine whether S_1 mixes with the higher-lying S_2 state outside the Franck−Condon region, we performed several additional analyses. First, we calculated the time evolution of the S_2-S_1 energy gap for 10 representative AIMS TBFs moving on the S_1 state before the first spawning event. This was performed for the OP1, OP2, OP3 in aqueous solution and OP2 in the β_1-AR and β_2-ARs. For most TBFs, the two states remain energetically separated for most of the time. Occasionally, the energy gap between the two states is close to or below 0.1 eV. (Figure S8), indicating potential mixing. However, such mixing did not trigger many $S_1 \rightarrow S_2$ spawning events in our AIMS calculations due to the low nonadiabatic coupling between these states. The S_2 state was explicitly included in the AIMS simulations, and the S_2 state population remains below 2% in all simulations (Figure S12). This result indicates that although mixing between S_1 and S_2 can occur along certain trajectories, its extent is minimal and does not strongly couple to the predominant $S_1 \rightarrow S_0$ population-transfer dynamics.

Additionally, we optimized the minimum-energy pathway on the S_1 state PES from the FC region to the S_1/S_0 MECI using the nudged elastic band (NEB) method, analyzed the weights of the dominant electronic configurations (Table S3), and plotted the molecular orbitals for images along the pathway (Figures S9−S11). The leading configurations of S_1 and S_2 remain different

Downloaded from pubs.acs.org/jctcce/article-pdf/doi/10.1021/acs.jctc.6c01210/6902145/3/acs.jctc.6c01210.pdf by TEXAS TECH UNIV user on 29 October 2026

https://doi.org/10.1021/acs.jctc.6c01210
J. Chem. Theory Comput. XXXX, XXX, XXX−XXX

along the pathway: the S_1 state is dominated initially by $n\pi^*$ character and later by mixing with the ground-state closed-shell configuration near the S_1/S_0 MECI, whereas the S_2 state is dominated initially by $\pi\pi^*$ character and later by $\pi\pi^*$ double-excitation character. Therefore, these results indicate that substantial S_1/S_2 mixing does not occur frequently during the relaxation, and the dynamics are dominated by evolution on S_1 toward the S_0/S_1 intersection with minimal nonadiabatic transitions to higher-lying states.

Relationship between Local Contacts and Excited-State Lifetime

To understand how ligand and receptor environments alter excited-state dynamics, we analyzed the average and averaged variance of the contact number around the ligand during the excited-state dynamics, i.e., $\bar{N}$ and $\overline{\sigma_N^2}$. These two quantities are averaged over all ICs for each AIMS simulation system. The contact number N is defined in the SI. The $\overline{\sigma_N^2}$ quantifies the fluctuations in the number of atoms forming van der Waals contacts with the ligand during excited-state dynamics in the AIMS simulation.[53,57] A smaller variance corresponds to a more rigid environment during the excited-state dynamics.[57] Our previous studies have shown that changes in contact-number fluctuations can modify the excited-state decay kinetics.[53,57,62]

In aqueous solution, OP3 exhibits the shortest τ and the smallest $\overline{\sigma_N^2}$ (Figure 5 and Table 2). This is possibly because the fast S_1-state dynamics leave little time for large rearrangements of the local environment in response to photoexcitation. The relationship between τ and $\overline{\sigma_N^2}$ can also be observed for the same ligand across β_2-AR mutants (Figure 5B–D and Table 2). For OP2, the D113E mutant is associated with the longest τ, consistent with the largest $\overline{\sigma_N^2}$. For both OP1 and OP3 in the β_2-AR variants, the WT has the longest τ and the largest $\overline{\sigma_N^2}$. These results indicate that faster excited-state decay kinetics are related to smaller fluctuations in local contact number. However, this is a qualitative relationship because some differences fall within the error bars. Our results indicate that ultrafast local rotation around the central N═N double bond does not require significant *a priori* rearrangement of the local environment to accommodate the torsional motion. Otherwise, large values of $\overline{\sigma_N^2}$ would have also been observed for shorter τ, which is inconsistent with the data above. This volume-conserving isomerization mechanism is highly analogous to that of retinal protonated Schiff bases in rhodopsins.[95,96]

Table 2. Average Contact Number ($\bar{N}$) and Variance of the Contact Number (σ_N^2) Calculated during the S_1-State Dynamics of the OP Photoswitches in the Aqueous Solution, β_2-AR, β_1-AR, and β_2-AR Mutants[a]

	Quantity	OP1	OP2	OP3
water	$\bar{N}$	118.2 ± 2.1	111.9 ± 1.9	117.6 ± 1.8
	$\overline{\sigma_N^2}$	65.0 ± 6.7	62.3 ± 6.7	54.6 ± 5.1
β_2-AR	$\bar{N}$	77.4 ± 1.1	67.1 ± 1.1	73.1 ± 1.1
	$\overline{\sigma_N^2}$	30.8 ± 2.9	27.6 ± 2.3	40.8 ± 4.3
β_1-AR	$\bar{N}$	52.8 ± 1.2	55.1 ± 1.1	59.4 ± 1.2
	$\overline{\sigma_N^2}$	16.2 ± 1.8	19.3 ± 1.9	24.6 ± 2.3
β_2-AR$_{F289A}$	$\bar{N}$	65.5 ± 0.9	63.7 ± 1.5	58.4 ± 1.5
	$\overline{\sigma_N^2}$	27.4 ± 3.4	31.2 ± 3.0	23.4 ± 2.2
β_2-AR$_{Y199A}$	$\bar{N}$	63.6 ± 1.6	73.7 ± 1.7	76.5 ± 1.1
	$\overline{\sigma_N^2}$	23.2 ± 2.8	30.0 ± 3.8	30.6 ± 3.9
β_2-AR$_{D113E}$	$\bar{N}$	N/A	64.3 ± 1.1	N/A
	$\overline{\sigma_N^2}$		39.4 ± 3.3	
β_2-AR$_{D113(P),WT}$	$\bar{N}$	N/A	73.9 ± 1.1	N/A
	$\overline{\sigma_N^2}$		33.1 ± 3.2	

[a]The result of WT β_2-AR with protonated D113 residue is also included (labeled as β_2-AR$_{D113(P),WT}$).

Furthermore, to identify which residues and local interactions are most closely related to the photoisomerization decay time, we further analyzed the average contact number $\bar{N}$ between the azobenzene moiety of OP2 and the nearby aromatic residues Y199 and F289 along the S_1-state AIMS TBFs. The azobenzene group interacts with both aromatic residues during the excited-state dynamics, but the contacts with Y199 show a much clearer relationship with the decay time constant. The average contact number between residue Y199 and the azobenzene moiety increases with the S_1-state decay time constant (τ) across the five OP2 systems, including WT β_2-AR, the F289A, Y199A, D113E, and WT β_2-AR with protonated D113 (Figure S13A), exhibiting a strong positive correlation (R^2 = 0.993) This result suggests that, between these two residues, the contact number with Y199 correlates more strongly with the S_1-state decay time constants. The D113E mutant provides a clear example of this behavior. Because the Glu113 side chain is longer than the Asp side chain in the WT receptor, the mutation shifts the position of OP2 in the binding pocket and brings the azobenzene group closer to Y199, as shown in Figure 4. Consistent with this structural change, the D113E system shows both the largest number of Y199-azobenzene contacts and the longest S_1-state lifetime.

Relationship between Torsional Dynamics during Nonadiabatic Transition and QY

To understand why the calculated QYs do not follow a simple relationship with the excited-state decay time constants, we first analyzed the distribution of the θ_{CNNC} torsional velocity of the S_0-state TBFs' centroids at the $S_1 \rightarrow S_0$ spawning time point, which marks the onset of the nonadiabatic transition and the decay of the S_1-state population to the ground state. The distributions are weighted by final populations of the S_0-state TBFs. Then, we analyzed the fraction of S_0-state TBF population initially moving in the positive torsional direction (generating the *trans*-isomer photoproduct) relative to the total S_0-state TBF population. This quantity represents the initial branching ratio of ground-state torsional dynamics, and correlates with the final QY (Figure 6). This trend is obvious for the OPs in aqueous solution and is also retained across β_2-AR and its mutants. This correlation is considerable for the protonation of the counterion at the D113 residue, which significantly increases the initial branching ratio of ground-state torsional dynamics and the resulting QY (Figure 6C) compared with the WT β_2-AR with a deprotonated D113 residue. Therefore, the QY is primarily determined by the direction of torsional dynamics immediately after the nonadiabatic transition. This explains why the excited-state decay time constant alone cannot predict photoisomerization quantum efficiency. A trajectory can rapidly reach the vicinity of the S_1/S_0 CI seam, but if the spawned ground-state TBF is not initially directed toward forming the *trans*-isomer product, it does not necessarily contribute to productive isomerization.

The backward-isomerization analysis provides additional information about this process. Table S4 shows the population

Downloaded from pubs.acs.org/jctcce/article-pdf/doi/10.1021/acs.jctc.6c01210/6902145/3/acs.jctc.6c01210.pdf by TEXAS TECH UNIV user on 29 October 2026

https://doi.org/10.1021/acs.jctc.6c01210
J. Chem. Theory Comput. XXXX, XXX, XXX−XXX

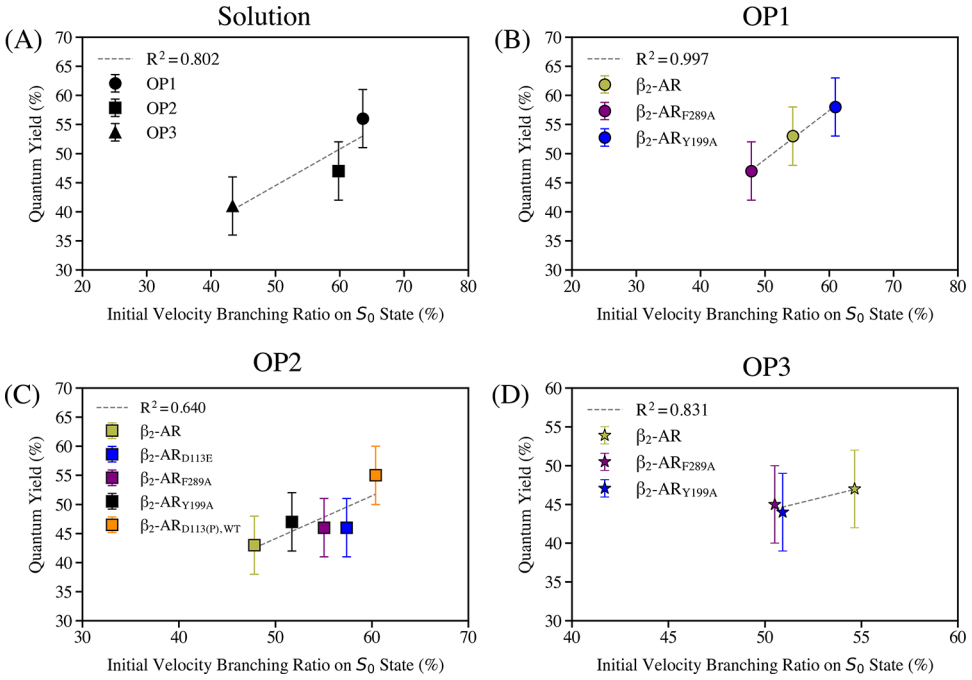


Figure 6. Relationship between the initial branching ratio of ground-state torsional dynamics and the isomerization QY. (A) Aqueous solution. (B) OP1 in WT β_2-AR and its mutants, (C) OP2 in WT β_2-AR and its mutants, (D) OP3 in WT β_2-AR and its mutants.

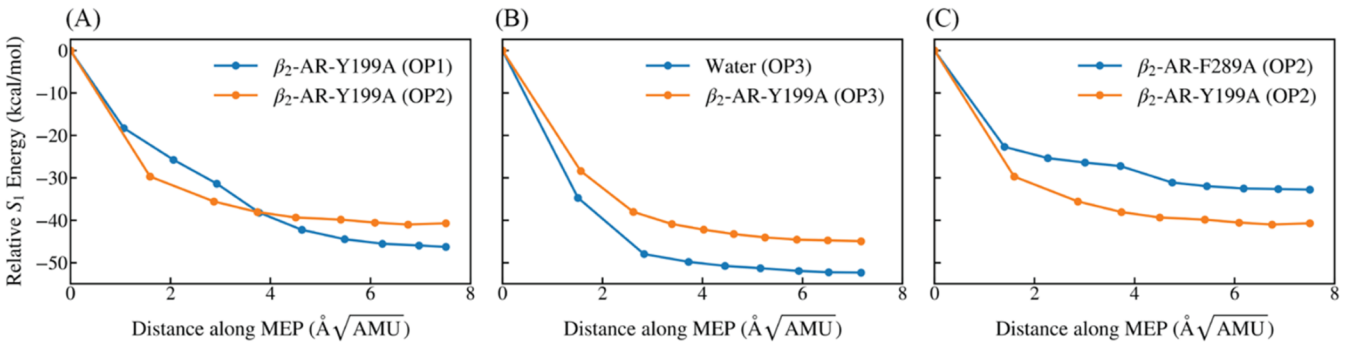


Figure 7. Minimum-energy pathways (MEPs) connecting representative Franck−Condon (FC) structures to the S_1/S_0 minimum-energy conical intersection (MECI) region are compared to illustrate the effects of (A) ligand substitution, (B) protein environment (water vs receptor), and (C) binding pocket mutation. Steeper downhill pathways generally correlate with faster excited-state relaxation on the excited-state PES. The *x*-axis shows mass-weighted cumulative distances along the MEP. The *y* axis shows the S_1-state energy of the images relative to the FC point.

fraction of ground-state TBFs that initially moved forward but eventually reversed their torsional velocity, returning to the *cis* reactant (backward isomerization). Mutations and chemical substituents both can change the extent of backward isomerization, altering the QY. However, backward isomerization usually accounts for less than 10% of the total S_0-state population (Table S4) and has a minor effect on the QY relative to the initial branching ratio of ground-state torsional dynamics. For example, OP2 in the F289A mutant of β_2-AR has a larger backward-isomerization population than OP2 in WT β_2-AR, while the two systems show similar QYs.

Relationship between Excited-State PES and Dynamics

To characterize how ligand substitution, receptor binding, and mutation reshape the excited-state energy landscape, we optimized the S_1-state minimum-energy pathways (MEPs) connecting representative Franck−Condon (FC) structures to the S_1/S_0 minimum-energy conical intersection (MECI). These MEP optimizations were performed using the nudged elastic band (NEB) method, where the PES were described at the hh-TDA-BH&HLYP/6−31G*/MM level of theory. During the optimizations of the FC, MECI, and pathways, the residues and solvent molecules within 5 Å of the ligand were allowed to relax, while the remainder of the environment was kept frozen.

Representative comparisons are illustrated in Figure 7, highlighting (A) the effect of ligand substitution, (B) the effect of the surrounding environment, and (C) the effect of receptor mutation. We also calculated the energy difference between FC and MECI on the S_1 state. Figure S14 illustrates the correlation between this energy difference and the relaxation time for all the systems.

The resulting energy profiles provide a qualitative connection between the shape of the excited-state PES and dynamics. In general, if the reaction pathway from the FC region toward the MECI has a larger energetic driving force, it is expected to lead to faster excited-state relaxation (Figure S14). This trend is particularly apparent for the Y199A mutant: OP1 exhibits the largest energy decrease (−45.94 kcal/mol) and the shortest relaxation time (70 ± 5 fs), whereas OP2 shows a smaller energy

Downloaded from pubs.acs.org/jctcce/article-pdf/doi/10.1021/acs.jctc.6c01210/6902145/acs.jctc.6c01210.pdf by TEXAS TECH UNIV user on 29 October 2026

https://doi.org/10.1021/acs.jctc.6c01210
J. Chem. Theory Comput. XXXX, XXX, XXX−XXX

decrease (−40.69 kcal/mol) and a longer relaxation time (113 ± 9 fs); OP3 displays intermediate behavior, with an energy decrease of −44.73 kcal/mol and a relaxation time of 84 ± 8 fs. A similar trend is observed for OP2 in different mutants: the smaller energy decrease in F289A (−32.64 kcal/mol) is accompanied by a longer relaxation time (136 ± 14 fs) compared with Y199A (−40.69 kcal/mol; 113 ± 9 fs). The differences are beyond the statistical uncertainties of the lifetimes.

In addition, comparison of OP3 in the aqueous solution and in the Y199A mutant of β_2-AR further illustrates that the FC-to-MECI energy decrease is not the sole factor controlling the relaxation dynamics, although it still plays an important role. OP3 in the aqueous solution exhibits a larger S_1 state energy decrease from FC to MECI (−52.31 kcal/mol) than in the Y199A mutant (−44.73 kcal/mol), but the corresponding relaxation times are essentially within the reported uncertainties (81 ± 6 and 84 ± 8 fs, respectively). This suggests that, while the S_1-state PES provides an important energetic driving force toward the crossing region, detailed features of the dynamics along the pathway can further modulate the relaxation lifetime. Therefore, the FC-to-MECI energy differences qualitatively correlate with the relaxation times, while the dynamics remain sensitive to additional environmental factors, such as steric and electrostatic effects.

Among the β_2-AR mutations, the D113E mutation has the largest effect on OP2 excited-state dynamics. The τ of OP2 substantially increases from 148 ± 24 fs in the WT β_2-AR to 238 ± 28 fs in the D113E mutant (Table 1). This slowdown is much larger than the changes observed in the F289A and Y199A mutants. Since the D113E introduces only a small perturbation in the side chain by adding one methylene ($-CH_2-$) group without changing the net charge, this mutant represents a distinct case for the mechanistic study of mutational effects on the excited-state dynamics.

To understand this unusually slow relaxation, we compared the S_1-state FC-to-MECI energy decrease. In WT β_2-AR, the S_1 energy decreases by 46.46 kcal/mol from the FC structure to the MECI region, indicating a substantial energetic driving force toward the vicinity of the S_1/S_0 MECI. In the D113E mutant, this energy decrease is reduced to 33.40 kcal mol^{-1}, corresponding to a 13.06 kcal mol^{-1} reduction in the overall driving force toward the MECI. This reduced FC-to-MECI gap is consistent with the much longer OP2 S_1 lifetime in the D113E mutant.

Relationship between Binding-Affinity Differential and QY

As hypothesized in our previous study,[3] the difference in the protein−ligand interactions between distinct isomeric forms of the same ligand can, in principle, affect the isomerization QY. A higher binding preference for the reactant tends to lower the photoisomerization QY. Meanwhile, a high binding affinity difference between the *cis* and *trans* isomers ($\Delta\Delta G_{binding,cis\rightarrow trans}$, referred to as "*cis*-vs-*trans* affinity differential") is key to the successful design of photoswitchable ligands, since it enhances the light-responsiveness of the ligand's bioactivity. The QY is also important because it is one of the key factors influencing the population ratio of different isomers at the photostationary state. Therefore, the relationship between $\Delta\Delta G_{binding,cis\rightarrow trans}$ and QY is crucial for understanding the trade-off between the two critical properties in the design of effective photoswitches targeting GPCRs: efficient photoisomerization and a large light-responsive binding affinity differential.

Here, we systematically examine such a correlation (Figure 8). The $\Delta\Delta G_{binding,cis\rightarrow trans}$ values are obtained from experimental

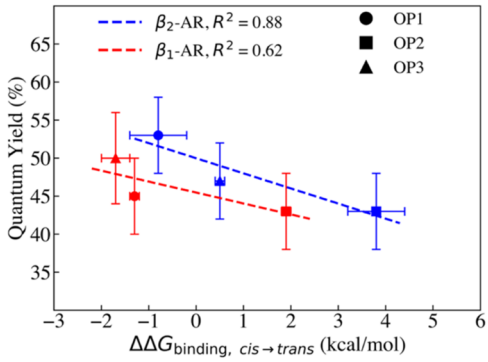


Figure 8. Correlation between the calculated *cis*-to-*trans* photoisomerization QYs and the experimental[22] $\Delta\Delta G_{binding,cis\rightarrow trans}$ for OP1, OP2, and OP3 in the WT β_1-AR and WT β_2-AR. Blue and red dashed lines show linear fits for β_2-AR and β_1-AR, respectively.

binding assays. Interestingly, in both β_1-AR and β_2-AR, a greater binding preference toward the *cis* isomer (more positive $\Delta\Delta G_{binding,cis\rightarrow trans}$) is associated with lower photoisomerization QY (Figure 8).[22] For example, OP2 exhibits the largest "*cis*-on" effect, and its *cis* → *trans* isomerization QY is the lowest. The trend suggests that the photochemical and thermodynamic properties of the OP photoswitches are closely connected. Thus, the substituent pattern affects the *cis*-vs-*trans* affinity differential and the quantum efficiency of the photoisomerization in a correlated manner. This leads to another major finding of this study: the same structural features that distinguish the binding affinities of the *cis* and *trans* forms on the ground-state free energy landscape also modulate the multistate torsional dynamics that induce nonadiabatic transitions, thereby influencing the isomerization QY.

Design Principles for Tuning Photoswitches Targeting β-ARs

Our results identify several practical design principles for tuning the photodynamics of photoswitches targeting β-AR. The first is optimizing the position of substituents where the azobenzene moiety connects to the IHP side chain. OP1, OP2, and OP3 contain the same azobenzene moiety and IHP side chain, but changing their attachment position changes how their photodynamics respond to receptor binding, receptor subtype, and pocket mutations. The substituent position therefore affects how protein−ligand interactions around the IHP side chain affect the local environment around the azobenzene moiety.

Second, tuning the hydrophobic interactions and hydrogen-bond network around the ligand significantly affects photodynamics. On one hand, local van der Waals interactions between the azobenzene group and nearby aromatic residues such as F289 and Y199 control its local packing and mainly affect the rate of excited-state relaxation. Mutating these residues to Ala generally shortens the S_1 lifetime. Similar changes could be introduced to the ligand by varying the size, position, or polarity of substituents on the azobenzene rings. On the other hand, changes in hydrogen-bond interactions around the IHP side chain can indirectly affect photodynamics by altering the packing of the azobenzene group with nearby hydrophobic residues. Protonating D113 increases the OP2 QY from 43 ± 5% to 55 ± 5%, and the D113E mutation strongly slows S_1-state population decay. These charged and polar protein−ligand

Downloaded from pubs.acs.org/jctcce/article-pdf/doi/10.1021/acs.jctc.6c01210/6902145/3/acs.jctc.6c01210.pdf by TEXAS TECH UNIV user on 29 October 2026

https://doi.org/10.1021/acs.jctc.6c01210
J. Chem. Theory Comput. XXXX, XXX, XXX−XXX

interactions may also be tuned through adjusting the basicity of the ligand's amine group, the length and rigidity of the linker, and modifying the IHP side chain's hydrogen-bond donors and acceptors through mutations. Moreover, this approach is also consistent with studies of retinal proteins,[97] where the excited-state pathway can be tuned by changing the protonation state of counterion residues or by redistributing the electrostatic field around the chromophore, even without major changes in steric confinement. Our results indicate that the location and spatial distribution of the electrostatic potential around the photoswitch can reshape the excited-state energy landscape and alter access to the nonadiabatic decay region, and such effects differ from neutralizing the charges of nearby counterions. This is supported by the results that the D113 residue's protonation and the D113E mutation have distinct effects on OP2 photodynamics and suggests that electrostatic-field organization around the chromophore should be treated as a design variable in GPCR photopharmacology.

These design principles are based on the ligand−receptor systems examined here and are most directly applicable to photoswitches with similar chemical structures and binding environments. Other photoswitches or receptor targets may respond differently and should therefore be evaluated individually.

CONCLUSION

In this work, we employed a multiscale framework incorporating first-principles nonadiabatic dynamics simulations in the QM/MM setting to investigate how chemical substitution, receptor subtype, binding-pocket mutation, and counterion charge neutralization regulate the ultrafast *cis*-to-*trans* photodynamics of OPs in β-ARs. It is worth noting that the systems under study are not arbitrarily chosen. The ligands and receptors examined here represent the most successful examples of class A GPCRs photopharmacology to date.[22,24] Also, the β-ARs, especially β_2-AR, are therapeutically important and have been extensively studied.

The calculated absorption spectra show that all OPs can be photoexcited through the $S_0 \rightarrow S_1$ transition, which is dominated by the $n\pi^*$ excitation. Thus, the protein environment does not fundamentally change the identity of the excited state. Chemical substitutions influence how the photodynamics of the ligands respond to receptor binding. The OP1, OP2, and OP3 exhibit different S_1-state lifetimes and *cis*-to-*trans* photoisomerization QYs in the aqueous solution, and the trend of excited-state lifetime is not correlated with the trend in QY. Binding with the WT β_2-AR changes the photodynamics of the OPs in a ligand-specific manner. Compared to the aqueous solution, upon receptor binding, the OP1 and OP2 have shorter S_1-state lifetimes, whereas OP3 has a longer lifetime. The response of QY to receptor binding is also ligand-dependent. Therefore, the substituent effect is not limited to spectra and photodynamics in the aqueous solution. It also determines how receptor binding changes excited-state dynamics, nonadiabatic relaxation, and photoproduct formation on the ground state.

Additionally, receptor-subtype and binding-pocket mutations, as well as protonation state changes, can perturb the excited-state dynamics and nonadiabatic transition leading to photoisomerization. The comparison between WT β_1-AR and WT β_2-AR shows that the receptor subtypes have nontrivial, ligand-specific effects on the photodynamics. OP1 is sensitive to switching receptor subtypes in terms of both excited-state lifetime and QY, whereas OP2 and OP3 show large changes in lifetime but only modest changes in QY. Local binding-pocket mutations in β_2-AR also can change photodynamics in a ligand-specific manner. The F289A and Y199A mutations generally accelerate the excited-state dynamics for all three OPs by reducing the number of contacts between the ligand's azobenzene moiety and the binding pocket residues, but their impact on QY is modest and ligand-dependent. The D113E mutation greatly slows OP2 excited-state decay but does not significantly perturb its QY.

The effects of neutralizing the D113 counterion's charge further demonstrate that perturbations in the electrostatic environment of the binding pocket can influence the photoisomerization QY. Protonation of the D113 residue only slightly changes OP2's S_1-state lifetime, but largely increases the QY. This indicates that charge perturbations are non-negligible even though the D113 residue does not directly interact with the azobenzene moiety of the ligand. The effect of the D113 residue's protonation likely arises from changes in the local hydrogen-bond network between the IHP side chain and D113, which shift the ligand's binding pose and the interactions between its azobenzene moiety with surrounding residues.

We also analyzed the geometric and energetic factors are correlated with the excited-state lifetime and QY. The local-contact-number analysis shows a qualitative relationship between the excited-state decay time constants and the average variance of the contact numbers, indicating that shorter excited-state lifetimes are related to smaller fluctuations in the contact number around the photoswitch. This finding suggests that ultrafast local rotation around the central N═N double bond does not require *a priori* rearrangement of the local environment, supporting a volume-conserving isomerization mechanism analogous to that of RPSB in rhodopsin. The unusually slow S_1-state decay of OP2 in the D113E mutant of the β_2-AR relative to the WT is explained by the reduced energy gap on the S_1-state PES between the FC region and the S_1/S_0 MECI, which weakens the driving force toward the vicinity of the S_1/S_0 CI seam space.

The isomerization QY is correlated with the initial branching ratio of ground-state torsional dynamics following the nonadiabatic transition. This indicates that productive photoisomerization is affected by whether the newly spawned ground-state TBF initially moves toward the *trans*-isomer product. The ground-state backward isomerization dynamics following the nonadiabatic transition play a minor role in determining the trend of QYs among different systems.

Finally, the isomerization QY has a qualitative relationship with the *cis*-vs-*trans* affinity differential. A greater binding preference toward the *cis* isomer is associated with a lower *cis*-to-*trans* isomerization QY in both β_1-AR and β_2-AR. This suggests that the same structural features that distinguish the binding affinities of the *cis* and *trans* isomers on the ground-state free-energy landscape also modulate torsional dynamics during nonadiabatic transitions among multiple electronic states.

Overall, through multiscale simulations, this study reveals that the ultrafast photodynamics of photoswitchable β-AR antagonists are affected by the coupled effects of multiple factors. Chemical substitution, receptor subtype, binding-pocket mutation, and counterion neutralization can influence the local electrostatic and steric environment in the binding pocket, thus perturbing the non-adiabatic dynamics of the ligands. These findings link the local molecular environments of receptor binding pockets to the photochemical properties of ligands, and provide new mechanistic insights into the photocontrol of cell

Downloaded from pubs.acs.org/jctcce/article-pdf/doi/10.1021/acs.jctc.6c01210/6902145/3/acs.jctc.6c01210.pdf by TEXAS TECH UNIV user on 29 October 2026

https://doi.org/10.1021/acs.jctc.6c01210
J. Chem. Theory Comput. XXXX, XXX, XXX−XXX

signaling via GPCRs beyond the scope of rhodopsins, informing general design principles for GPCR photopharmacology.

■ ASSOCIATED CONTENT

Data Availability Statement

The data underlying this study are available in the published article and the Supporting Information.

Supporting Information

The Supporting Information is available free of charge at https://pubs.acs.org/doi/10.1021/acs.jctc.6c01210.

Simulation setup for β_1-AR, validation of representative IC selection for AIMS simulations, convergence analysis of S_1 population dynamics, calculated UV−vis absorption spectra and comparisons with experiment, distributions of spawning times, analyses of S_1−S_2 energy gaps and electronic configurations, S_2 population dynamics, and correlations of excited-state lifetimes with local contact numbers and FC-to-MECI energy differencesSimulation setup for β_1-AR, validation of representative IC selection for AIMS simulations, convergence analysis of S_1 population dynamics, calculated UV−vis absorption spectra and comparisons with experiment, distributions of spawning times, analyses of S_1−S_2 energy gaps and electronic configurations, S_2 population dynamics, and correlations of excited-state lifetimes with local contact numbers and FC-to-MECI energy differences. (Figures S1−S14); $S_0 \rightarrow S_1$ excitation energies at absorption maxima, convergence of S1-state decay time constants, electronic configuration weights, backward-isomerization populations, and benchmark calculations at MECIs (Tables S1−S5), and definition of the local contact number (PDF)

Simulation setups, coordinates of the systems, along with the scripts and codes used to perform the simulations and analyze the resulting data (Sample Files) (ZIP)

■ AUTHOR INFORMATION

Corresponding Author

Ruibin Liang − *Department of Chemistry and Biochemistry, Texas Tech University, Lubbock, Texas 79409, United States;* orcid.org/0000-0001-8741-1520; Email: rliang@ttu.edu

Authors

Mohammad Khavani − *Department of Chemistry and Biochemistry, Texas Tech University, Lubbock, Texas 79409, United States*

Amirhossein Bakhtiiari − *Department of Chemistry and Biochemistry, Texas Tech University, Lubbock, Texas 79409, United States*

Complete contact information is available at: https://pubs.acs.org/10.1021/acs.jctc.6c01210

Author Contributions

†M.K. and A.B. contributed equally to this work.

Notes

The authors declare no competing financial interest.

■ ACKNOWLEDGMENTS

This work was supported by the National Institutes of Health (grant number: R35GM150780) and the Texas University Fund (TUF) for the Human Molecular Aging Center at Texas Tech University under internal award #TUF6656. We also acknowledge the computing facilities provided by the High-Performance Computing Center at Texas Tech University.

■ REFERENCES

(1) Segatta, F.; Cupellini, L.; Garavelli, M.; Mennucci, B. Quantum Chemical Modeling of the Photoinduced Activity of Multichromophoric Biosystems. *Chem. Rev.* **2019**, *119* (16), 9361−9380.

(2) Gozem, S.; Luk, H. L.; Schapiro, I.; Olivucci, M. Theory and Simulation of the Ultrafast Double-Bond Isomerization of Biological Chromophores. *Chem. Rev.* **2017**, *117* (22), 13502−13565.

(3) Liang, R.; Bakhtiiari, A. Multiscale simulation unravels the light-regulated reversible inhibition of dihydrofolate reductase by phototrexate. *J. Chem. Phys.* **2022**, *156* (24), No. 245102.

(4) Liang, R.; Yu, J. K.; Meisner, J.; Liu, F.; Martinez, T. J. Electrostatic control of photoisomerization in channelrhodopsin 2. *J. Am. Chem. Soc.* **2021**, *143* (14), 5425−5437.

(5) Scholz, F.; Bamberg, E.; Bamann, C.; Wachtveitl, J. Tuning the Primary Reaction of Channelrhodopsin-2 by Imidazole, pH, and Site-Specific Mutations. *Biophys. J.* **2012**, *102* (11), 2649−2657.

(6) Martínez, T. J. Insights for Light-Driven Molecular Devices from Ab Initio Multiple Spawning Excited-State Dynamics of Organic and Biological Chromophores. *Acc. Chem. Res.* **2006**, *39* (2), 119−126.

(7) Palombo, R.; Barneschi, L.; Pedraza-González, L.; Padula, D.; Schapiro, I.; Olivucci, M. Retinal chromophore charge delocalization and confinement explain the extreme photophysics of Neorhodopsin. *Nat. Commun.* **2022**, *13* (1), No. 6652.

(8) Barneschi, L.; Marsili, E.; Pedraza-González, L.; Padula, D.; De Vico, L.; Kaliakin, D.; Blanco-González, A.; Ferré, N.; Huix-Rotllant, M.; Filatov, M.; Olivucci, M. On the fluorescence enhancement of arch neuronal optogenetic reporters. *Nat. Commun.* **2022**, *13* (1), No. 6432.

(9) Sacchetta, F.; Yang, X.; Olivucci, M. Rhodopsin charge diffusion computations disclose contrasting color-tuning mechanisms. *Nat. Commun.* **2025**, *16* (1), No. 5534.

(10) del Carmen Marín, M.; Agathangelou, D.; Orozco-Gonzalez, Y.; Valentini, A.; Kato, Y.; Abe-Yoshizumi, R.; Kandori, H.; Choi, A.; Jung, K.-H.; Haacke, S.; Olivucci, M. Fluorescence Enhancement of a Microbial Rhodopsin via Electronic Reprogramming. *J. Am. Chem. Soc.* **2019**, *141* (1), 262−271.

(11) Demoulin, B.; Altavilla, S. F.; Rivalta, I.; Garavelli, M. Fine Tuning of Retinal Photoinduced Decay in Solution. *J. Phys. Chem. Lett.* **2017**, *8* (18), 4407−4412.

(12) El-Tahawy, M. M. T.; Nenov, A.; Weingart, O.; Olivucci, M.; Garavelli, M. Relationship between Excited State Lifetime and Isomerization Quantum Yield in Animal Rhodopsins: Beyond the One-Dimensional Landau−Zener Model. *J. Phys. Chem. Lett.* **2018**, *9* (12), 3315−3322.

(13) Church, J. R.; Amoyal, G. S.; Borin, V. A.; Adam, S.; Olsen, J. M. H.; Schapiro, I. Deciphering the Spectral Tuning Mechanism in Proteorhodopsin: The Dominant Role of Electrostatics Instead of Chromophore Geometry. *Chem. - Eur. J.* **2022**, *28* (28), No. e202200139.

(14) Toker, Y.; Langeland, J.; Gruber, E.; Kjær, C.; Nielsen, S. B.; Andersen, L. H.; Borin, V. A.; Schapiro, I. Counterion-controlled spectral tuning of the protonated Schiff-base retinal. *Phys. Rev. A* **2018**, *98* (4), No. 043428.

(15) Vengris, M.; van der Horst, M. A.; Zgrablić, G.; van Stokkum, I. H.; Haacke, S.; Chergui, M.; Hellingwerf, K. J.; van Grondelle, R.; Larsen, D. S. Contrasting the excited-state dynamics of the photoactive yellow protein chromophore: Protein versus solvent environments. *Biophys. J.* **2004**, *87* (3), 1848−1857.

(16) Rupenyan, A. B.; Vreede, J.; van Stokkum, I. H.; Hospes, M.; Kennis, J. T.; Hellingwerf, K. J.; Groot, M. L. Proline 68 enhances photoisomerization yield in photoactive yellow protein. *J. Phys. Chem. B* **2011**, *115* (20), 6668−6677.

(17) Toh, K. C.; Stojković, E. A.; van Stokkum, I. H.; Moffat, K.; Kennis, J. T. Fluorescence quantum yield and photochemistry of

Downloaded from pubs.acs.org/jctcce/article-pdf/doi/10.1021/acs.jctc.6c01210/6902145/acs.jctc.6c01210.pdf by TEXAS TECH UNIV user on 29 October 2026

bacteriophytochrome constructs. *Phys. Chem. Chem. Phys.* **2011**, *13* (25), 11985−11997.
(18) Salvadori, G.; Macaluso, V.; Pellicci, G.; Cupellini, L.; Granucci, G.; Mennucci, B. Protein control of photochemistry and transient intermediates in phytochromes. *Nat. Commun.* **2022**, *13* (1), No. 6838.
(19) Fischer, T.; Köhler, L.; Engel, P. D.; Song, C.; Gärtner, W.; Wachtveitl, J.; Slavov, C. Conserved tyrosine in phytochromes controls the photodynamics through steric demand and hydrogen bonding capabilities. *Biochim. Biophys. Acta, Bioenerg.* **2023**, *1864* (4), No. 148996.
(20) Zhou, Y.; Tang, S.; Chen, Z.; Zhou, Z.; Huang, J.; Kang, X.-W.; Zou, S.; Wang, B.; Zhang, T.; Ding, B.; Zhong, D. Origin of the multiphasic quenching dynamics in the BLUF domains across the species. *Nat. Commun.* **2024**, *15* (1), No. 623.
(21) Wijtmans, M.; Josimovic, I.; Vischer, H. F.; Leurs, R. Optical control of Class A G protein-coupled receptors with photoswitchable ligands. *Curr. Opin. Pharmacol.* **2022**, *63*, No. 102192.
(22) Bosma, R.; Dijon, N. C.; Zheng, Y.; Schihada, H.; Hauwert, N. J.; Shi, S.; Arimont, M.; Riemens, R.; Custers, H.; van de Stolpe, A.; Vischer, H. F.; Wijtmans, M.; Holliday, N. D.; Kuster, D. W. D.; Leurs, R. Optical control of the β2-adrenergic receptor with opto-prop-2: A cis-active azobenzene analog of propranolol. *iScience* **2022**, *25* (9), No. 104882.
(23) Duran-Corbera, A.; Catena, J.; Otero-Viñas, M.; Llebaria, A.; Rovira, X. Photoswitchable Antagonists for a Precise Spatiotemporal Control of β2-Adrenoceptors. *J. Med. Chem.* **2020**, *63* (15), 8458−8470.
(24) Shi, S.; Zheng, Y.; Goulding, J.; Marri, S.; Lucarini, L.; Konecny, B.; Sgambellone, S.; Villano, S.; Bosma, R.; Wijtmans, M.; Briddon, S. J.; Zarzycka, B. A.; Vischer, H. F.; Leurs, R. A high-affinity, cis-on photoswitchable beta blocker to optically control β2-adrenergic receptors in vitro and in vivo. *Biochem. Pharmacol.* **2024**, *226*, No. 116396.
(25) Ricart-Ortega, M.; Font, J.; Llebaria, A. GPCR photopharmacology. *Mol. Cell. Endocrinol.* **2019**, *488*, 36−51.
(26) Cao, Y.; Shi, S.; Does, S. A. H.; Buzink, C. M. L.; Gao, M.; de Esch, I. J. P.; Vischer, H. F.; Wijtmans, M.; Leurs, R. Photo-clenbuterol: Optical Control of β2-Adrenergic Receptor Signaling by Photoswitchable Ligand Efficacy. *J. Med. Chem.* **2025**, *68*, No. 12911.
(27) Donthamsetti, P.; Konrad, D. B.; Hetzler, B.; Fu, Z.; Trauner, D.; Isacoff, E. Y. Selective Photoswitchable Allosteric Agonist of a G Protein-Coupled Receptor. *J. Am. Chem. Soc.* **2021**, *143* (24), 8951−8956.
(28) Donthamsetti, P. C.; Broichhagen, J.; Vyklicky, V.; Stanley, C.; Fu, Z.; Visel, M.; Levitz, J. L.; Javitch, J. A.; Trauner, D.; Isacoff, E. Y. Genetically Targeted Optical Control of an Endogenous G Protein-Coupled Receptor. *J. Am. Chem. Soc.* **2019**, *141* (29), 11522−11530.
(29) Binkhorst, L. C. P.; Josimovic, I.; De Boer, B.; Simon, I. A.; Van Der Aa, F.; Zarzycka, B. A.; De Esch, I. J. P.; Vischer, H. F.; Windhorst, A. D.; Wijtmans, M.; Leurs, R. A Radiolabeled Photoswitchable G Protein-Coupled Receptor Antagonist Enlightens Ligand Binding Kinetics Associated with Photoswitching. *J. Am. Chem. Soc.* **2025**, *147* (27), 23991−24000.
(30) Frank, J. A.; Yushchenko, D. A.; Hodson, D. J.; Lipstein, N.; Nagpal, J.; Rutter, G. A.; Rhee, J.-S.; Gottschalk, A.; Brose, N.; Schultz, C.; Trauner, D. Photoswitchable diacylglycerols enable optical control of protein kinase C. *Nat. Chem. Biol.* **2016**, *12* (9), 755−762.
(31) Berry, M. H.; Holt, A.; Levitz, J.; Broichhagen, J.; Gaub, B. M.; Visel, M.; Stanley, C.; Aghi, K.; Kim, Y. J.; Cao, K.; Kramer, R. H.; Trauner, D.; Flannery, J.; Isacoff, E. Y. Restoration of patterned vision with an engineered photoactivatable G protein-coupled receptor. *Nat. Commun.* **2017**, *8* (1), No. 1862.
(32) Donthamsetti, P. C.; Winter, N.; Schönberger, M.; Levitz, J.; Stanley, C.; Javitch, J. A.; Isacoff, E. Y.; Trauner, D. Optical Control of Dopamine Receptors Using a Photoswitchable Tethered Inverse Agonist. *J. Am. Chem. Soc.* **2017**, *139* (51), 18522−18535.
(33) Morstein, J.; Hill, R. Z.; Novak, A. J. E.; Feng, S.; Norman, D. D.; Donthamsetti, P. C.; Frank, J. A.; Harayama, T.; Williams, B. M.; Parrill, A. L.; Tigyi, G. J.; Riezman, H.; Isacoff, E. Y.; Bautista, D. M.; Trauner, D. Optical control of sphingosine-1-phosphate formation and function. *Nat. Chem. Biol.* **2019**, *15* (6), 623−631.
(34) Hüll, K.; Morstein, J.; Trauner, D. In Vivo Photopharmacology. *Chem. Rev.* **2018**, *118* (21), 10710−10747.
(35) Stipp, R.; Bertrand, Q.; Trabuco, M.; Duran-Corbera, A.; Ignazzitto, M. T.; Glover, H.; Stierli, F.; Catena, J.; Carrillo, M.; Hartmann, S.; Seidel, H.-P.; Mulder, M.; Mason, T.; Kondo, Y.; Wranik, M.; Appleby, M.; Sager, C.; Sierra, R.; Gate, G.; Schleissner, P.; Cheng, X.; Weinert, T.; Cheng, R.; Mous, S.; Beale, J. H.; Kepa, M.; Llebaria, A.; Hennig, M.; Rovira, X.; Standfuss, J. Structural Mechanism of an Efficacy Photoswitch Targeting the β2-adrenergic Receptor. *Angew. Chem., Int. Ed.* **2026**, *65*, No. e17995.
(36) Glover, H.; Saßmannshausen, T.; Bertrand, Q.; Trabuco, M.; Slavov, C.; Bacchin, A.; Andres, F.; Kondo, Y.; Stipp, R.; Wranik, M.; Khusainov, G.; Carrillo, M.; Kekilli, D.; Nan, J.; Gonzalez, A.; Cheng, R.; Neidhart, W.; Weinert, T.; Leonarski, F.; Dworkowski, F.; Kepa, M.; Wachtveitl, J.; Hennig, M.; Standfuss, J. Photoswitch dissociation from a G protein-coupled receptor resolved by time-resolved serial crystallography. *Nat. Commun.* **2024**, *15* (1), No. 10837.
(37) Saßmannshausen, T.; Glover, H.; Trabuco, M.; Neidhart, W.; Cheng, R.; Hennig, M.; Slavov, C.; Standfuss, J.; Wachtveitl, J. Kinetic Basis for the Design of Azobenzene-Based Photoswitchable A2a Adenosine Receptor Ligands. *J. Am. Chem. Soc.* **2024**, *146* (47), 32670−32677.
(38) Szymanski, W.; Beierle, J. M.; Kistemaker, H. A.; Velema, W. A.; Feringa, B. L. Reversible photocontrol of biological systems by the incorporation of molecular photoswitches. *Chem. Rev.* **2013**, *113* (8), 6114−6178.
(39) Lefkowitz, R. J. Seven transmembrane receptors—A brief personal retrospective. *Biochim. Biophys. Acta, Biomembr.* **2007**, *1768* (4), 748−755.
(40) Santos, R.; Ursu, O.; Gaulton, A.; Bento, A. P.; Donadi, R. S.; Bologa, C. G.; Karlsson, A.; Al-Lazikani, B.; Hersey, A.; Oprea, T. I.; Overington, J. P. A comprehensive map of molecular drug targets. *Nat. Rev. Drug Discovery* **2017**, *16* (1), 19−34.
(41) Khavani, M.; Bakhtiiari, A.; Khalvati, L.; Leurs, R.; Liang, R. A Systematic Benchmark Study of Free Energy Methods for Quantifying Light-Responsive Binding Affinities of Photoswitchable Antagonists of Beta-Adrenergic Receptors. *J. Med. Chem.* **2026**, *69*, No. 9265, DOI: 10.1021/acs.jmedchem.5c03756.
(42) Cederbaum, L. S.Born−Oppenheimer Approximation and Beyond. In *Conical Intersections: Electronic Structure, Dynamics and Spectroscopy*; World Scientific Publishing, 2004; Vol. *15*, pp 3−40 .
(43) Reed, P. M. M.; Jang, J.; Woloschuk, R. M.; Reis, J.; Hille, J. I.; Uppalapati, M.; Woolley, G. A. Effects of binding partners on thermal reversion rates of photoswitchable molecules. *Proc. Natl. Acad. Sci. U.S.A.* **2025**, *122* (10), No. e2414748122.
(44) Broichhagen, J.; Frank, J. A.; Trauner, D. A Roadmap to Success in Photopharmacology. *Acc. Chem. Res.* **2015**, *48* (7), 1947−1960.
(45) Kazim, M.; Yoo, E. Recent Advances in the Development of Non-Invasive Imaging Probes for Cancer Immunotherapy. *Angew. Chem., Int. Ed.* **2024**, *63* (2), No. e202310694.
(46) Kobauri, P.; Dekker, F. J.; Szymanski, W.; Feringa, B. L. Rational Design in Photopharmacology with Molecular Photoswitches. *Angew. Chem., Int. Ed.* **2023**, *62* (30), No. e202300681.
(47) Sahoo, J.; Sahoo, S.; Subramaniam, Y.; Bhatt, P.; Rana, S.; De, M. Photo-Controlled Gating of Selective Bacterial Membrane Interaction and Enhanced Antibacterial Activity for Wound Healing. *Angew. Chem.* **2024**, *136* (1), No. e202314804.
(48) Liu, R.; Yao, J.; Zhou, S.; Yang, J.; Zhang, Y.; Yang, X.; Li, L.; Zhang, Y.; Zhuang, Y.; Yang, Y.; Chen, X. Spatiotemporal control of RNA metabolism and CRISPR−Cas functions using engineered photoswitchable RNA-binding proteins. *Nat. Protoc.* **2024**, *19* (2), 374−405.
(49) Axelrod, S.; Shakhnovich, E.; Gómez-Bombarelli, R. Mapping the Space of Photoswitchable Ligands and Photodruggable Proteins with Computational Modeling. *J. Chem. Inf. Model.* **2023**, *63* (18), 5794−5802.

Downloaded from pubs.acs.org/jctcce/article-pdf/doi/10.1021/acs.jctc.6c01210/6902145/3/acs.jctc.6c01210.pdf by TEXAS TECH UNIV user on 29 October 2026

(50) Stranius, K.; Börjesson, K. Determining the photoisomerization quantum yield of photoswitchable molecules in solution and in the solid state. *Sci. Rep.* **2017**, *7* (1), No. 41145.
(51) Rastogi, S. K.; Zhao, Z.; Barrett, S. L.; Shelton, S. D.; Zafferani, M.; Anderson, H. E.; Blumenthal, M. O.; Jones, L. R.; Wang, L.; Li, X.; Streu, C. N.; Du, L.; Brittain, W. J. Photoresponsive azo-combretastatin A-4 analogues. *Eur. J. Med. Chem.* **2018**, *143*, 1−7.
(52) Rosenbaum, D. M.; Rasmussen, S. G.; Kobilka, B. K. The structure and function of G-protein-coupled receptors. *Nature* **2009**, *459* (7245), 356−363.
(53) Bakhtiiari, A.; Khavani, M.; Costa, G. J.; Liang, R. A Multiscale Simulation Framework for Elucidating Photochemical Structure−Activity Relationships of Photoswitchable Ligands in Complex Biomolecular Environments. *J. Chem. Inf. Model.* **2025**, *65* (23), 12861−12878.
(54) Ben-Nun, M.; Quenneville, J.; Martínez, T. J. Ab initio multiple spawning: Photochemistry from first principles quantum molecular dynamics. *J. Phys. Chem. A* **2000**, *104* (22), 5161−5175.
(55) Ben-Nun, M.; Martínez, T. J.Ab Initio Quantum Molecular Dynamics. In *Advances in Chemical Physics*; John Wiley & Sons, 2002; Vol. *121*, pp 439−512 .
(56) Curchod, B. F. E.; Martínez, T. J. Ab initio nonadiabatic quantum molecular dynamics. *Chem. Rev.* **2018**, *118* (7), 3305−3336.
(57) Liang, R.; Bakhtiiari, A. Effects of enzyme−ligand interactions on the photoisomerization of a light-regulated chemotherapeutic drug. *J. Phys. Chem. B* **2022**, *126* (12), 2382−2393.
(58) Yu, J. K.; Bannwarth, C.; Hohenstein, E. G.; Martínez, T. J. Ab initio nonadiabatic molecular dynamics with hole−hole Tamm−Dancoff approximated density functional theory. *J. Chem. Theory Comput.* **2020**, *16* (9), 5499−5511.
(59) Yu, J. K.; Bannwarth, C.; Liang, R.; Hohenstein, E. G.; Martínez, T. J. Nonadiabatic dynamics simulation of the wavelength-dependent photochemistry of azobenzene excited to the nπ^* and $\pi\pi^*$ excited states. *J. Am. Chem. Soc.* **2020**, *142* (49), 20680−20690.
(60) Liang, R. First-principles nonadiabatic dynamics simulation of azobenzene photodynamics in solutions. *J. Chem. Theory Comput.* **2021**, *17* (5), 3019−3030.
(61) Bakhtiiari, A.; Costa, G. J.; Liang, R. On the Simulation of Thermal Isomerization of Molecular Photoswitches in Biological Systems. *J. Chem. Theory Comput.* **2023**, *19* (18), 6484−6499.
(62) Bakhtiiari, A.; Liang, R. Unraveling Solvent and Substituent Effects in the Photodynamics of Light-Dependent Microtubule Inhibitors for Cancer Phototherapy. *J. Comput. Chem.* **2025**, *46* (7), No. e70076.
(63) Liang, R.; Das, D.; Bakhtiiari, A. Protein confinement fine-tunes aggregation-induced emission in human serum albumin. *Phys. Chem. Chem. Phys.* **2021**, *23* (46), 26263−26272.
(64) Ishchenko, A.; Stauch, B.; Han, G. W.; Batyuk, A.; Shiriaeva, A.; Li, C.; Zatsepin, N.; Weierstall, U.; Liu, W.; Nango, E.; et al. Toward G protein-coupled receptor structure-based drug design using X-ray lasers. *IUCrJ* **2019**, *6* (6), 1106−1119.
(65) Xu, X.; Kaindl, J.; Clark, M. J.; Hübner, H.; Hirata, K.; Sunahara, R. K.; Gmeiner, P.; Kobilka, B. K.; Liu, X. Binding pathway determines norepinephrine selectivity for the human β1AR over β2AR. *Cell Res.* **2021**, *31* (5), 569−579.
(66) Manna, M.; Kulig, W.; Javanainen, M.; Tynkkynen, J.; Hensen, U.; Müller, D. J.; Rog, T.; Vattulainen, I. How to minimize artifacts in atomistic simulations of membrane proteins, whose crystal structure is heavily engineered: β2-adrenergic receptor in the spotlight. *J. Chem. Theory Comput.* **2015**, *11* (7), 3432−3445.
(67) Webb, B.; Sali, A. Comparative protein structure modeling using MODELLER. *Curr. Protoc. Bioinf.* **2016**, *54* (1), 5−6.
(68) Trott, O.; Olson, A. J. AutoDock Vina: improving the speed and accuracy of docking with a new scoring function, efficient optimization, and multithreading. *J. Comput. Chem.* **2010**, *31* (2), 455−461.
(69) Anandakrishnan, R.; Aguilar, B.; Onufriev, A. V. H++ 3.0: automating p K prediction and the preparation of biomolecular structures for atomistic molecular modeling and simulations. *Nucleic Acids Res.* **2012**, *40* (W1), W537−W541.
(70) Wu, E. L.; Cheng, X.; Jo, S.; Rui, H.; Song, K. C.; Dávila-Contreras, E. M.; Qi, Y.; Lee, J.; Monje-Galvan, V.; Venable, R. M. *CHARMM-GUI Membrane Builder toward Realistic Biological Membrane Simulations*; Wiley Online Library, 2014.
(71) Hanson, M. A.; Cherezov, V.; Griffith, M. T.; Roth, C. B.; Jaakola, V.-P.; Chien, E. Y.; Velasquez, J.; Kuhn, P.; Stevens, R. C. A specific cholesterol binding site is established by the 2.8 Å structure of the human β2-adrenergic receptor. *Structure* **2008**, *16* (6), 897−905.
(72) Cherezov, V.; Rosenbaum, D. M.; Hanson, M. A.; Rasmussen, S. G.; Thian, F. S.; Kobilka, T. S.; Choi, H.-J.; Kuhn, P.; Weis, W. I.; Kobilka, B. K.; Stevens, R. C. High-resolution crystal structure of an engineered human β2-adrenergic G protein−coupled receptor. *Science* **2007**, *318* (5854), 1258−1265.
(73) Jorgensen, W. L.; Chandrasekhar, J.; Madura, J. D.; Impey, R. W.; Klein, M. L. Comparison of simple potential functions for simulating liquid water. *J. Chem. Phys.* **1983**, *79* (2), 926−935.
(74) Maier, J. A.; Martinez, C.; Kasavajhala, K.; Wickstrom, L.; Hauser, K. E.; Simmerling, C. ff14SB: improving the accuracy of protein side chain and backbone parameters from ff99SB. *J. Chem. Theory Comput.* **2015**, *11* (8), 3696−3713.
(75) Skjevik, Å. A.; Madej, B. D.; Dickson, C. J.; Lin, C.; Teigen, K.; Walker, R. C.; Gould, I. R. Simulation of lipid bilayer self-assembly using all-atom lipid force fields. *Phys. Chem. Chem. Phys.* **2016**, *18* (15), 10573−10584.
(76) Wang, J.; Wang, W.; Kollman, P. A.; Case, D. A. Automatic atom type and bond type perception in molecular mechanical calculations. *J. Mol. Graphics Modell.* **2006**, *25* (2), 247−260.
(77) Wang, J.; Wolf, R. M.; Caldwell, J. W.; Kollman, P. A.; Case, D. A. Development and testing of a general amber force field. *J. Comput. Chem.* **2004**, *25* (9), 1157−1174.
(78) Seritan, S.; Bannwarth, C.; Fales, B. S.; Hohenstein, E. G.; Kokkila-Schumacher, S. I.; Luehr, N.; Snyder, J. W.; Song, C.; Titov, A. V.; Ufimtsev, I. S.; Martínez, T. J. TeraChem: Accelerating electronic structure and ab initio molecular dynamics with graphical processing units. *J. Chem. Phys.* **2020**, *152* (22), No. 224110, DOI: 10.1063/5.0007615.
(79) Seritan, S.; Bannwarth, C.; Fales, B. S.; Hohenstein, E. G.; Isborn, C. M.; Kokkila-Schumacher, S. I.; Li, X.; Liu, F.; Luehr, N.; Snyder, J. W., Jr; et al. TeraChem: A graphical processing unit-accelerated electronic structure package for large-scale ab initio molecular dynamics. *WIREs Comput. Mol. Sci.* **2021**, *11* (2), No. e1494.
(80) Uberuaga, B. P.; Anghel, M.; Voter, A. F. Synchronization of trajectories in canonical molecular-dynamics simulations: Observation, explanation, and exploitation. *J. Chem. Phys.* **2004**, *120* (14), 6363−6374.
(81) Sindhikara, D. J.; Kim, S.; Voter, A. F.; Roitberg, A. E. Bad seeds sprout perilous dynamics: Stochastic thermostat induced trajectory synchronization in biomolecules. *J. Chem. Theory Comput.* **2009**, *5* (6), 1624−1631.
(82) Darden, T.; York, D.; Pedersen, L. Particle mesh Ewald: An N log (N) method for Ewald sums in large systems. *J. Chem. Phys.* **1993**, *98*, 10089.
(83) Ryckaert, J.-P.; Ciccotti, G.; Berendsen, H. J. Numerical integration of the cartesian equations of motion of a system with constraints: molecular dynamics of n-alkanes. *J. Comput. Phys.* **1977**, *23* (3), 327−341.
(84) Case, D. A.; Aktulga, H. M.; Belfon, K.; Ben-Shalom, I. Y.; Berryman, J. T.; Brozell, S. R.; Cerutti, D. S.; Cheatham, T. E., III; Cisneros, G. A.; Cruzeiro, V. W. D. *Amber 2023*; University of California: San Francisco, 2023.
(85) Ufimtsev, I. S.; Martinez, T. J. Quantum chemistry on graphical processing units. 3. Analytical energy gradients, geometry optimization, and first principles molecular dynamics. *J. Chem. Theory Comput.* **2009**, *5* (10), 2619−2628.
(86) Titov, A. V.; Ufimtsev, I. S.; Luehr, N.; Martinez, T. J. Generating efficient quantum chemistry codes for novel architectures. *J. Chem. Theory Comput.* **2013**, *9* (1), 213−221.
(87) Durant, J. L. Evaluation of transition state properties by density functional theory. *Chem. Phys. Lett.* **1996**, *256* (6), 595−602.

Downloaded from pubs.acs.org/jctcce/article-pdf/doi/10.1021/acs.jctc.6c01210/6902453/acs.jctc.6c01210.pdf by TEXAS TECH UNIV user on 29 October 2026

(88) Jones, C. M.; List, N. H.; Martínez, T. J. Steric and Electronic Origins of Fluorescence in GFP and GFP-like Proteins. *J. Am. Chem. Soc.* **2022**, *144* (28), 12732−12746.
(89) Eastman, P.; Friedrichs, M. S.; Chodera, J. D.; Radmer, R. J.; Bruns, C. M.; Ku, J. P.; Beauchamp, K. A.; Lane, T. J.; Wang, L.-P.; Shukla, D.; et al. OpenMM 4: a reusable, extensible, hardware independent library for high performance molecular simulation. *J. Chem. Theory Comput.* **2013**, *9* (1), 461−469.
(90) Barbatti, M.; Aquino, A. J.; Lischka, H. The UV absorption of nucleobases: semi-classical ab initio spectra simulations. *Phys. Chem. Chem. Phys.* **2010**, *12* (19), 4959−4967.
(91) Curchod, B. F. E.; Sisto, A.; Martínez, T. J. Ab Initio Multiple Spawning Photochemical Dynamics of DMABN Using GPUs. *J. Phys. Chem. A* **2017**, *121* (1), 265−276.
(92) Barbatti, M.; Aquino, A. J. A.; Lischka, H. The UV absorption of nucleobases: semi-classical ab initio spectra simulations. *Phys. Chem. Chem. Phys.* **2010**, *12* (19), 4959−4967.
(93) Liang, R.; Liu, F.; Martínez, T. J. Nonadiabatic Photodynamics of Retinal Protonated Schiff Base in Channelrhodopsin 2. *J. Phys. Chem. Lett.* **2019**, *10* (11), 2862−2868.
(94) Yu, J. K.; Liang, R.; Liu, F.; Martínez, T. J. First-Principles Characterization of the Elusive I Fluorescent State and the Structural Evolution of Retinal Protonated Schiff Base in Bacteriorhodopsin. *J. Am. Chem. Soc.* **2019**, *141* (45), 18193−18203.
(95) Warshel, A. Bicycle-pedal model for the first step in the vision process. *Nature* **1976**, *260*, 679−683.
(96) Liu, R. S. H. Photoisomerization by Hula-Twist: A Fundamental Supramolecular Photochemical Reaction. *Acc. Chem. Res.* **2001**, *34* (7), 555−562.
(97) Walisinghe, D.; Sacchetta, F.; Olivucci, M. Theoretical principles for designing fluorescent rhodopsins: Electrostatic control of excited-state pathways. *Chem. Phys. Rev.* **2026**, *7* (2), No. 021311, DOI: 10.1063/5.0339458.

Downloaded from pubs.acs.org/jctcce/article-pdf/doi/10.1021/acs.jctc.6c01210/6902145 3/acs.jctc.6c01210.pdf by TEXAS TECH UNIV user on 29 October 2026